Ore Geology Reviews 136 (2021) 104259

Contents lists available at ScienceDirect

Ore Geology Reviews

journal homepage: www.elsevier.com/locate/oregeorev

# Contribution of microbial processes to the enrichment of Middle Permian manganese deposits in northern Guizhou, South China

Wenchao Yu [a,b,*], Márta Polgári [c,d,*], Krisztián Fintor [e], Ildikó Gyollai [c], Máté Szabó [c], Felicitász Velledits [f], Zhichen Liu [b,g], Yuansheng Du [b,h]

[a] State Key Laboratory of Geological Processes and Mineral Resource, School of Earth Sciences, China University of Geosciences, Wuhan 430074, China
[b] Innovation Center of Ore Resources Exploration Technology in the Region of Bedrock, Ministry of Natural Resources of People's Republic of China, Guiyang 550004, China
[c] Institute for Geological and Geochemical Research, Research Centre for Astronomy and Earth Sciences, ELRN, 1112 Budapest, Budaörsi str. 45, Hungary
[d] Department of Natural Geography and Geoinformatics, Eszterházy Károly University, 3300 Eger, Leányka str. 6, Hungary
[e] Dept. of Mineralogy, Geochemistry and Petrology, University of Szeged, 6722 Szeged, Egyetem str. 2-6, Hungary
[f] Mineralogical-Geological Institute, Miskolc University, Egyetemváros 3515, Miskolc, Hungary
[g] 102 Geological Brigade, Guizhou Bureau of Geology and Mineral Exploration and Development, Zunyi 563099, China
[h] State Key Laboratory of Biogeology and Environmental Geology, School of Earth Sciences, China University of Geosciences, Wuhan 430074, China

ARTICLE INFO

*Keywords:*
Geomicrobiology
Maokou formation
Mn-metasomatism
Rhodochrosite
Anatase
Marcasite

ABSTRACT

Economically important manganese deposits are hosted in the Middle Permian Maokou Formation of Zunyi, northern Guizhou, South China. During the Middle Permian, the intense rifting related to the initial stage of the Emeishan Large Igneous Province (ELIP) led to the development of carbonate platforms and inter-platform troughs. The manganese deposits occur in the transitional zone between carbonate platforms and troughs. Previous studies emphasized that the hydrothermal activities at the bottom of the trough basin controlled the formation of manganese deposits. In this study, new sedimentary, mineralogical, and stable isotope evidence are acquired from this manganese deposit, indicating that the microbially-mediated metallogenic mechanism also made an important contribution for the Middle Permian manganese deposition. The metallogenesis of this manganese deposit is highly like the combination of hydrothermal and microbial processes. Manganese ores in Zunyi are manganese carbonate, showing massive and clastic structures, no macroscopic nor microscopic lamination are found, samples are coarse-grained, diagenetically recrystallized with abundant mineralized microbial and microfossil biosignatures. FTIR, EPMA, and Raman analyses recognize micrometer-scale cyclic mineralogical assembly and help reconstruct the proposed new model of microbial manganese metallogenesis. Hydrothermal activity in the basin provided dissolved $Mn^{2+}$ ions into the anoxic basal watermass. In the syngenetic stage, microbial systems could be subdivided into three categories: (1) cyanobacterial system, (2) Mn-biomat system and (3) Fe-biomat system. Cyanobacterial activity led to the precipitation of calcite, and it could be partially affected by Mn-metasomatism and transformed to Mn-bearing calcite. Mn-oxidizing microbes led to the precipitation of manganese bio-oxide ($\delta$-$MnO_2$) near the redoxcline of the basin. Fe-biomat system was responsible for the precipitation of Fe-oxides (hematite) and Fe-hydroxides (ferrihydrite and lepidocrocite). After burial, manganese oxides reacted with the organic matter in the sediments through the microbially-mediated processes during the early diagenesis and the Mn-metasomatism of the cyanobacterial carbonate jointly contributed to formation of early diagenetic manganese carbonate ore. The redox fluctuations between oxic/suboxic and anoxic zones led to the re-oxidation process and resulted in cyclic marcasite. Anatase cycles observed in samples were interpreted as the diagenetic product of Fe-biomat system.

* Corresponding authors at: State Key Laboratory of Geological Processes and Mineral Resource, School of Earth Sciences, China University of Geosciences, Wuhan 430074, China (W. Yu). Institute for Geological and Geochemical Research, Research Centre for Astronomy and Earth Sciences, ELRN, 1112 Budapest, Budaörsi str. 45, Hungary (M. Polgári).
*E-mail addresses:* yuwenchaocug@163.com (W. Yu), rodokrozit@gmail.com (M. Polgári).

https://doi.org/10.1016/j.oregeorev.2021.104259
Received 9 January 2021; Received in revised form 9 May 2021; Accepted 23 May 2021
Available online 25 May 2021

## 1. Introduction

As a general framework, based on our experiences on demand of Mn and Fe deposit formation we found that the syngenetic situation (double microbial ore forming system – suboxic in the case of Fe and oxic in the case of Mn – is similar, but the result is variable outlook of deposits concerning mineralogy (in Mn deposits Fe is in the shadow, in Fe deposits Mn is in the shadow). Naturally metal source is needed. Geodynamic situation refer to rifting (or failed rifting) zone, and distal hydrothermal discharge. What cause differences? Among others, accumulation ratio differences (if the accumulation is slow, a part of the organic matter will be oxidized by atmospheric oxygen, and less amount of reactive organic matter will be buried), mass balance differences (accumulating organic matter (type and mass), metal oxide concentration and type, other forming minerals, etc.). We can surf from site to site through geological time, till now the results support the above detailed conditions (Polgári et al., 2012a, 2012b; Bodor et al., 2016; Molnár et al., 2017; Yu et al., 2019; Polgári et al., 2019, 2012a, 2012b; Biondi et al., 2020 current volume; Yu et al., 2021 current volume). The oxygen supply can be the result of currents, cyanobacterial ventilation (Yu et al., 2019a, 2019b). Further, these are starving basins, because if there is a considerable debris contribution, microbial biomat system will be destroyed, or diluted. Further, such systems provide information on paleoenvironmental conditions (Eh, pH).

Formation ages of sedimentary manganese deposits in China range from Mesoproterozoic to Quaternary (Fan and Yang, 1999). In South China, several important manganese deposits occurred in Neoproterozoic, Ordovician, Devonian, Carboniferous, Permian and Triassic strata (Fan and Yang, 1999; Xu et al., 2019). The Zunyi manganese metallogenic belt outcrops occurs in the northern Guizhou Province, southwestern China and extents to the western boundary of Guizhou, where a series of large to medium scale manganese deposits are concentrated in this metallogenic belt with a total manganese reserve larger than 150 million tons (Fig. 1A B). The manganese deposits are preserved in the Middle Permian Maokou Formation. Recent geochronology study constrains the age of manganese deposits to >263 Ma, according to the zircon U-Pb ages from the overlying claystone and the conodont biostratigraphic zone (Yan et al., 2020). Thus the formation age of manganese deposits should be before Middle Capitanian Stage.

Late Middle Permian (Capitanian) witnessed some drastic changes in the Earth's geological history, including the eruption of Emeishan Large Igneous Province (ELIP) (Zhong et al., 2007; Xu et al., 2008; Shellnutt, 2014; Shellnutt et al., 2020), the Guadalupian mass extinction (Day et al., 2015; Rampino and Shen, 2019), and the global regression event (Isozaki et al., 2007; Kofukuda et al., 2014). The onset of volcanism of the ELIP started from ca. 263 Ma, probably began from submarine volcanism and the consequent violent, phreatomagmatic-style eruptions (Jerram et al., 2016; Yan et al., 2020). It then transited to voluminous flood volcanism during the main eruption stage (He et al., 2007), and covered >30,000 km$^2$. Magmatic activities of ELIP may last for ~7 myr (263–256 Ma), and caused the regional uplift in the central zone of ELIP due to the axisymmetric doming and consequent uplift and rifting in the central and adjacent areas (He et al., 2010; Wang et al., 2018). At the end of Guadalupian, a mass extinction event happened, although the ages of the marine extinction remain unclear but mostly occured at ~260 Ma (Jin et al., 1995; Day et al., 2015), thus it coincided with the activities of ELIP, the low global sea-level and the low Sr isotope record in the marine deposits (Korte and Ullmann, 2018). Reasons of the extinction event could be complicated: the severe environmental crisis in marine (e.g., anoxic and acidification) played an important role for the losses of ~70% species in marine invertebrates (Isozaki and Servais, 2018) and at least 56% of plant species (Day et al., 2015). Rapid sea-level fallen happened during the Capitanian and it reached its minimum to the Phanerozoic around the Guadalupian (Middle Permian)–Lopingian (Late Permian) boundary, causing the widespread disconformity in sedimentary sequences (Isozaki et al., 2008; Kofukuda et al., 2014). This sea-level decline probably indicates the cooling event during the transition from the late Paleozoic icehouse to the Mesozoic greenhouse regime (Isozaki et al., 2007).

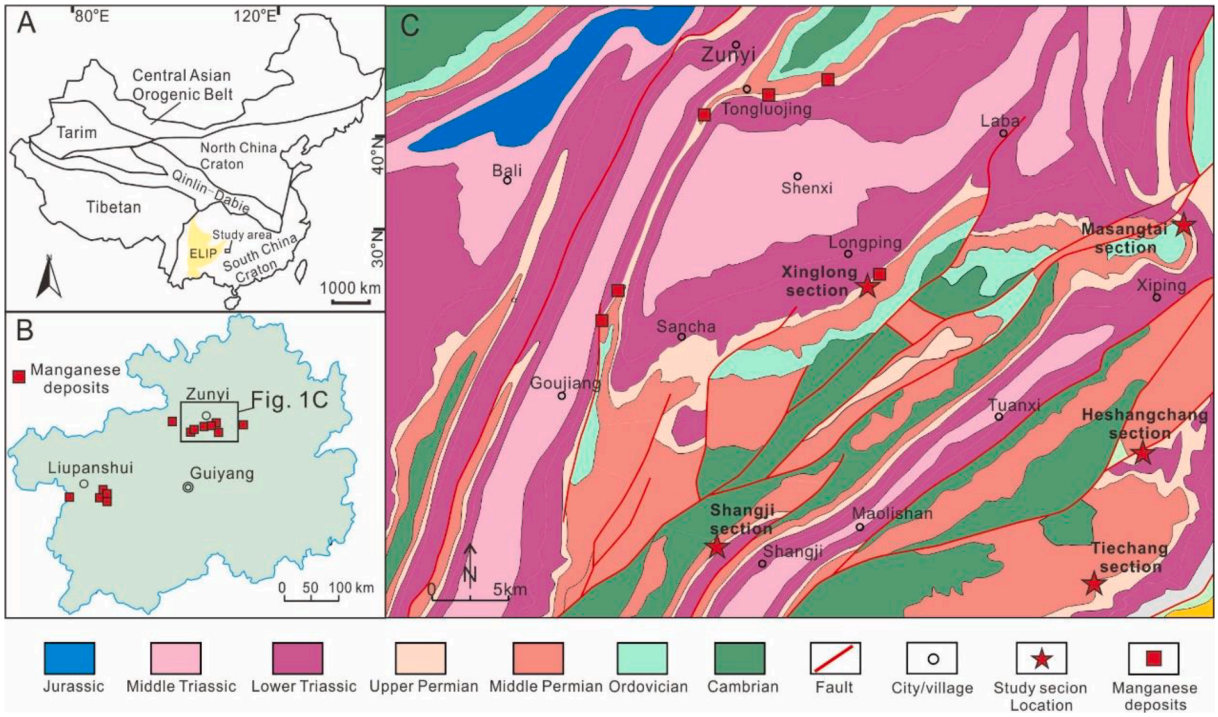


**Fig. 1.** A-Location of study area in China and the main tectonic subregions of China; B-Main manganese mining deposits and the study area in Guizhou Province, South China; C-Geological map of the southern Zunyi area, Guizhou, South China, stars mark the studying sections. ELIP in Fig. 1A = Emeishan Large Igneous Provence.

Previous studies on the Middle Permian manganese deposits in Zunyi emphasized the key role of the hydrothermal activities in the manganese-forming basins. A series of evidence support this argument, including: (1) lamellar, massive, banded, and brecciated structures of ore (Xu et al., 2019); (2) hydrothermal paragenetic gangue minerals, e.g., rutile, barite, pyrite, and chalcopyrite (Gao et al., 2018); (3) REEs of manganese ores are characterized by enrichments of La, Ce, Nd and Y ((e.g., monazite and xenotime; Liu et al., 2008, 2015; Xu et al., 2019); and (4) elements discrimination diagrams indicate the hydrothermal source for manganese deposits (Gao et al., 2018). In these studies, some clues imply the strong geobiological activities during the formation of the manganese deposits in Zunyi, such as the abundant organic matter, micro-laminae, and nodules in the manganese ores (Liu et al., 2015; Gao et al., 2018). Recently, evidences of the microbially mediated manganese metallogenesis have been widely reported in the ancient (Precambrian to Mesozoic) and modern manganese deposit (Blöthe et al., 2015; Polgári et al., 2019; Yu et al., 2019b; Biondi et al., 2020). The background information about the role of microorganisms in the formation of sedimentary deposits are given in detail in Polgári and Gyollai (2021 current volume). The Permian basin in Zunyi, South China perfectly accord with the favorable conditions for formation of manganese deposits: It was located in the rifting zone with strong basal hydrothermal activities (Xu et al., 2019), the redox condition transformed from anoxic to oxic-anoxic (Xu et al., 2021), and most important, high productivity and intense microbial activities (Shi et al., 2016). These clues lead to the possibility of contribution of microbial processes to the enrichment of manganese deposit in Zunyi.

In this study, we elaborate the re-examination of the manganese ore samples in the manganese deposit of Zunyi, northern Guizhou, South China. Based on new evidence achieved from petrological, mineralogical, geochemical and stable isotopic analyses, microbially-mediated mechanism as metal enrichment factor is proposed to be a "missing link" between the hydrothermal manganese source and the manganese deposits.

## 2. Geological setting

The study area is in the western South China Block (Fig. 1A). A series of Permian manganese deposits have been discovered in the NNE-trending in Guizhou Province (Fig. 1B). Due to a series of tectonic movements from Paleozoic to Mesozoic [e.g., Guangxi (a Late Ordovician to Late Silurian tectonic movement in the South China Block), the Indochina and the Himalaya movements], Silurian, Devonian, Late Triassic and Cretaceous strata are absent in this area (Fig. 1C). During the Early Permian to Middle Permian, the South China Block was in the low-latitude area, the sedimentary sequence in the block was dominated by shallow marine carbonate deposits (Yu et al., 2019a). During Late Middle Permian, sedimentary differentiation began to develop in the South China Block and led to the coexistence of carbonate platforms and inter-platform troughs. This sedimentary differentiation was reflected in the lithology and thickness variations of the Maokou Formation. The Maokou Formation can be divided into three members in the study area (Fig. 2): (1) the 1st Member is mainly composed of massive and thick bioclastic limestone with siliceous nodules and lenses, with thickness of 100 – 150 m; (2) the 2nd Member is dominated by thin carbonaceous limestone, siliceous limestone and siliceous rock, with thickness of 10 – 80 m; and (3) the 3rd Member in the carbonate platform environment is the bioclastic and micritic limestone, while in the interplatform trough basin environment, thin-layer siliceous rock developed. Manganese deposits (Mn-bearing carbonate) occurred in the transitional zone between interplatform trough and the carbonate platform and in the interplatform trough (Liu et al., 2019). Thickness of the manganese deposit is <10 m. Based on the conodont fossils in the Maokou Formation of Zunyi, the Maokou Formation started the deposition at the Middle Wordian (Middle Guadalupian) and terminated during the end of Capitanian (Bgmrhnp, 1988). Between the Maokou Formation and the overlying

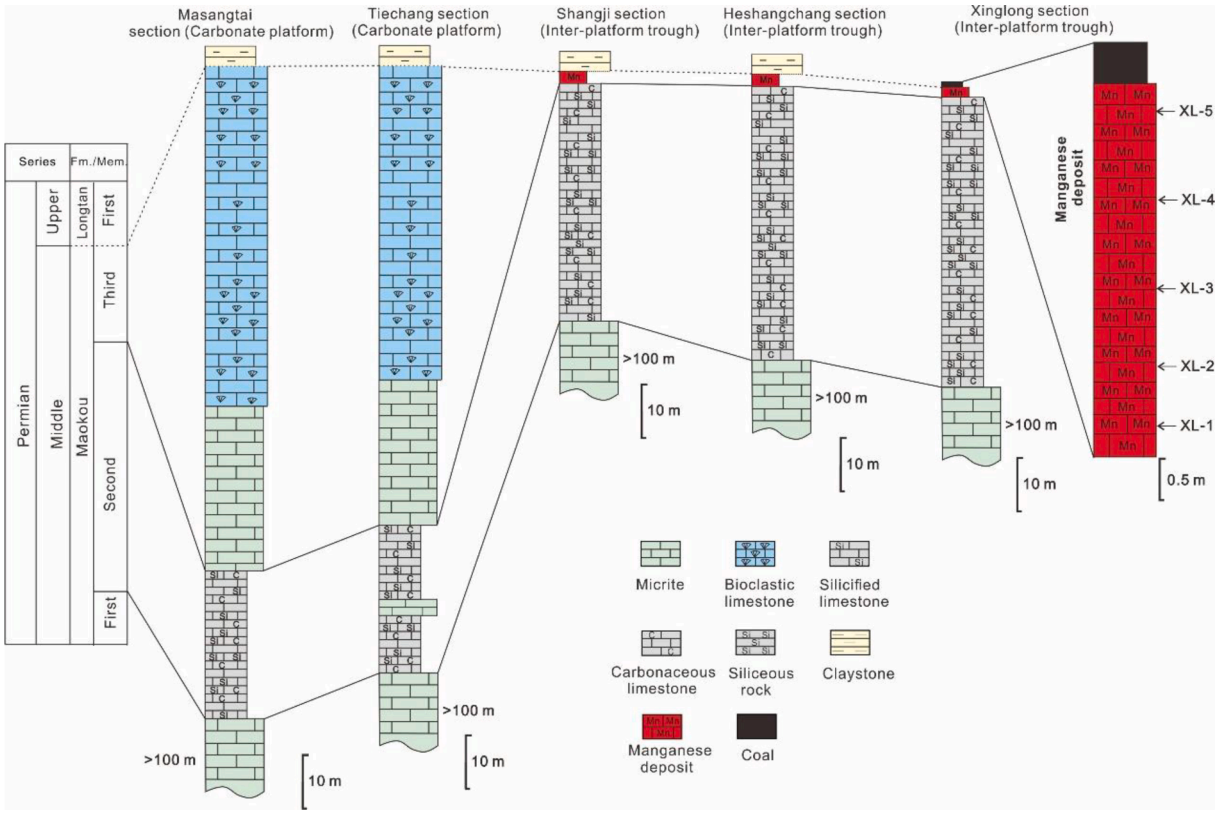


**Fig. 2.** Lithological columns of the Maokou Formation in the Masangtai, Tiechang, Shangji, Hehsangchang and Xinglong sections, the manganese deposit in the Xinglong section is magnified and showing the sampling positions. Locations of these sections are shown in Fig. 1.

Longtan Formation, there is a parallel unconformity, indicating the sedimentary hiatus around the Guadalupian-Lopingian Boundary (GLB).

Changes of thickness and lithology of the Maokou Formation imply the carbonate platform to the deep-water trough co-existed during Middle Permian, and the final exposure indicate that the study area went through the swift sea-level decline during the transition of Middle-Later Permian. Activities of the ELIP and the consequent tectonic effects are likely the major factor controlling the regional sea-level changes. The early stage of the ELIP accompanied with the submarine volcanic eruptions (Jerram et al., 2016; Yan et al., 2020) and the rifting system in the western South China Block (Wang et al., 2018). However, the tectonic background of the western South China Block during early period of the ELIP is still in debate. Previous studies contribute it to the early subsidence of lithosphere due to the mantle plume activities (Wang et al., 2018), a recent study argues that the western South China Block was still in the back-arc region of the Permian Paleo-Tethys subduction zone at that time (Zhu et al., 2019). The exposure surface on the topmost Maokou Formation indicates a sudden regression, which reflects a major global sea-level drop at the GLB (Isozaki et al., 2008; Kofukuda et al., 2014), and it was reinforced in the South China Block by regional crustal doming linked to ELIP emplacement (He et al., 2010).

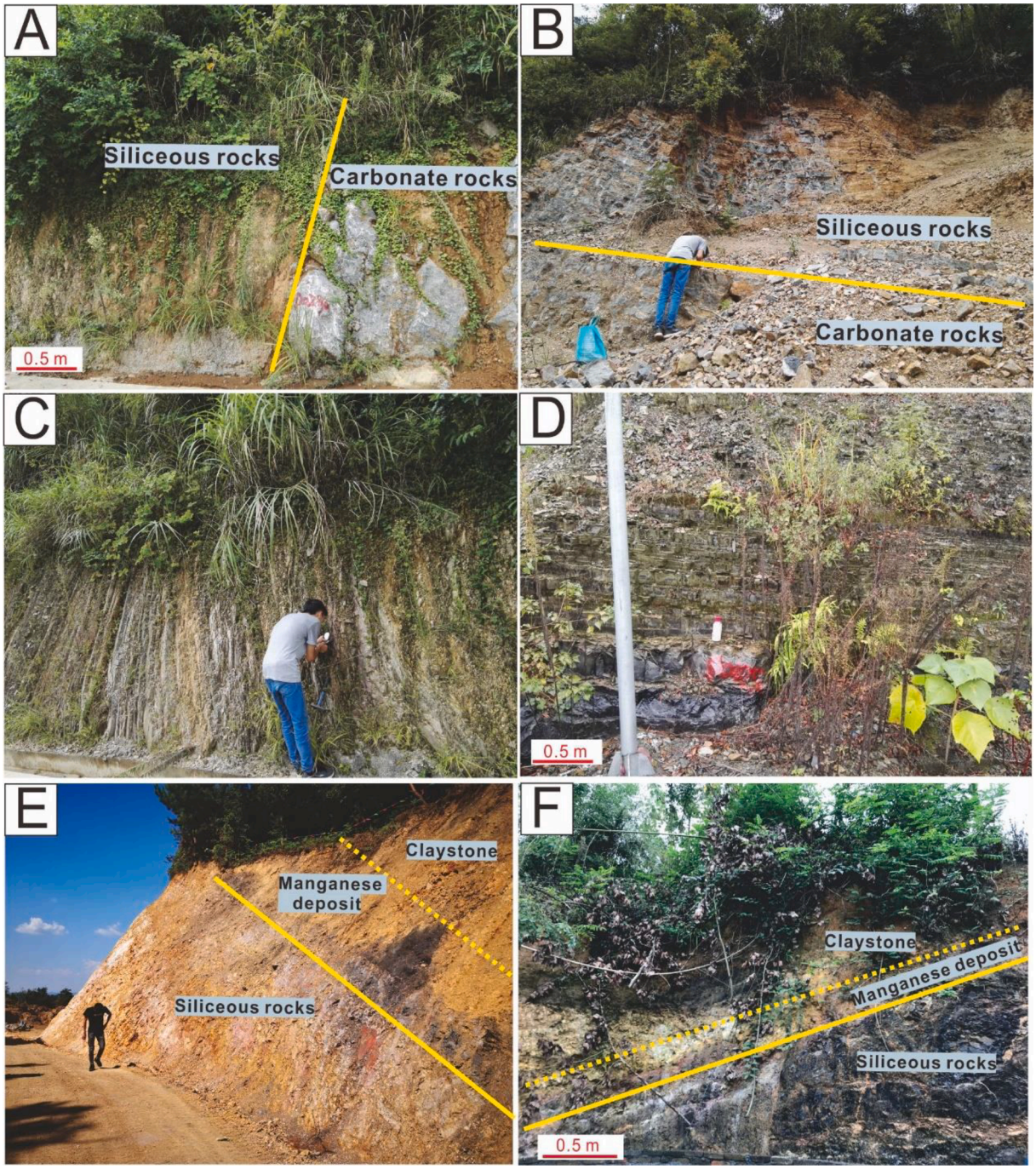


**Fig. 3.** Field photos of the sections in this study. A, B-The boundary between the 1st Member and the 2nd Member of the Maokou Formation in the Xinglong section and the Heshangchang section, respectively; C, D-Siliceous rocks in the 2nd Member of the Maokou Formation in the Xinglong section and the Heshangchang section, respectively; E, F-Manganese deposit in the 3rd Member of the Maokou Formation in the Xinglong section and the Heshangchang section, respectively.

## 3. Sampling

Totally five sections (Masangtai, Tiechang, Xinglong, Shangji, Heshangchang) are analyzed in this study, both are located in southeast of Zunyi city, northern Guizhou (Fig. 1). The Masangtai and Tiechang sections (Fig. 2) are represent the typical carbonate platform deposits of the Maokou Formation. Three members of the Maokou Formation are well preserved in two sections: the 1st Member is massive and thick bioclastic and micritic limestone with scattered siliceous nodules, the thickness of this Member is 100–110 m; the 2nd Member consists of ~20-m-thick siliceous limestone and carbonaceous limestone with interbedded thin siliceous layers; the 3rd Member returns to the carbonate deposit, containing 60 to 70-m-thick bioclastic and micritic limestones. No manganese deposit is found in Masangtai and Tiechang sections, the Maokou Formation is overlain by the white claystone of the Upper Permian Longtan Formation. The Shangji, Heshangchang and

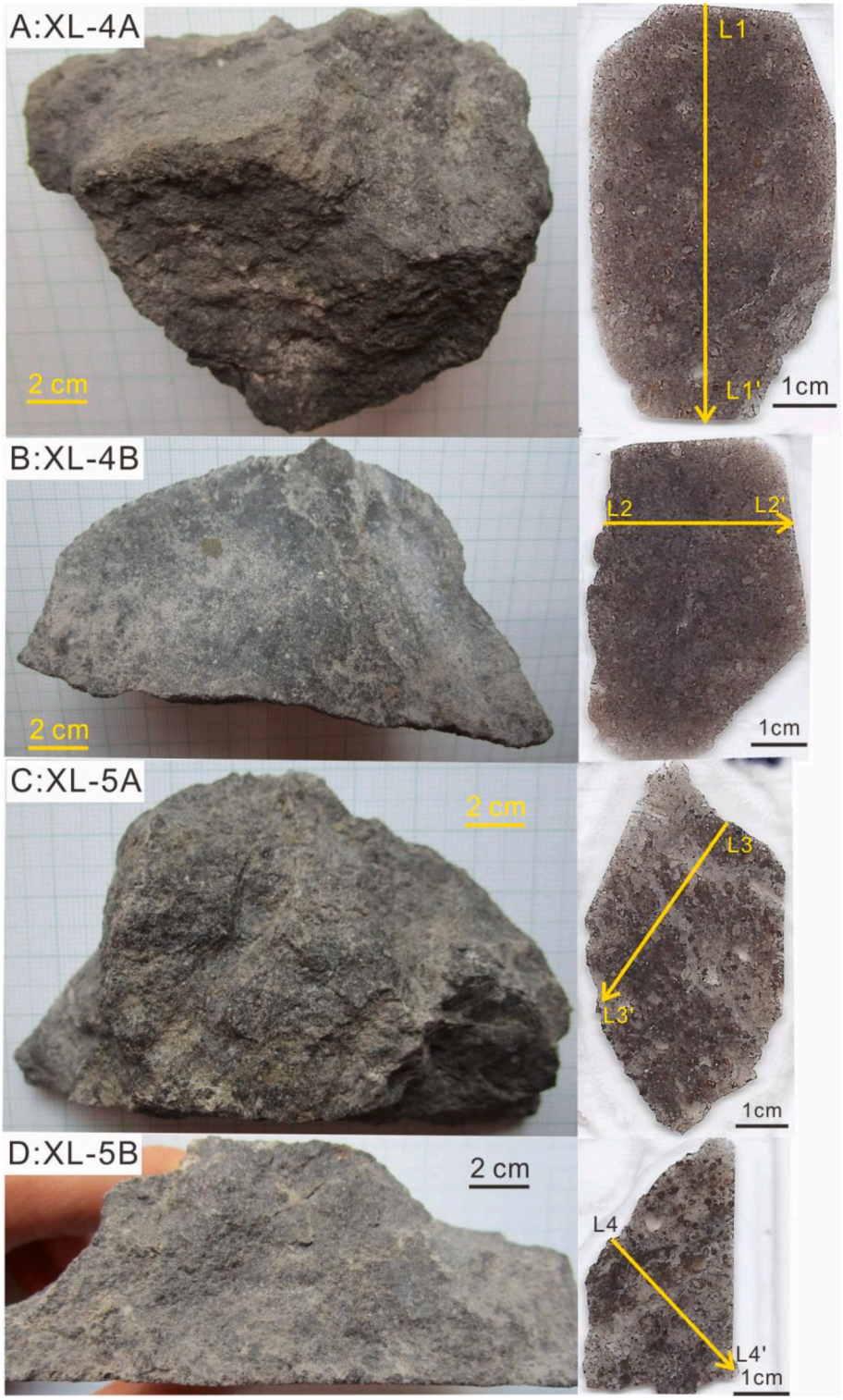


**Fig. 4.** Typical samples and thin sections from the manganese deposit of the middle Permian Maokou Formation in the Xinglong section. A, B- Sample XL-4; C, D-Sample XL-5. Yellow lines indicate the analyses pathways, arrows show the moving direction.

Xinglong sections all contain manganese deposit, representing by the Xinglong section, three sections show similar lithological features (Fig. 2 and Fig. 3). The Xinglong section is ~3 km southeast of Longping village, the 1st and 2nd members of the Maokou Formation in the Xinglong section is similar with the Masangtai and Tiechang sections, being composed of limestone and siliceous limestone, respectively (Fig. 3A B C D). The 3rd Member of the Maokou Formation in the Xinglong section is a 3-m-thick black manganese-bearing carbonate deposit, with massive, clastic and laminated structures (Fig. 3E F). However, in different sections, thickness of the manganese deposits show variation, for example, in the Heshangchang section, thickness of the manganese deposit is only about 0.5 m. All surficial manganese deposits in the field show strong weathering, and the manganese carbonate deposits have transformed into manganese oxides deposits. Thus we chose the fresh, unaltered samples from the mining underground tunnel for this study. Totally five samples (XL-1 to XL-5 in ascending order) were taken from the manganese deposit of the Xinglong section with equal interval (~0.6 m, Fig. 2).

Collected samples are massive dark gray or black, fine- to coarse-grained manganese carbonate ore with diagenetic sedimentary features, lacking of macroscopically visible lamination (Fig. 4). Two representative manganese ore samples (XL-4 and XL-5) were sent to Institute for Geological and Geochemical Research, Hungary for further analyses (Table S1). From the rock samples four thin sections were made (XL-4A, XL-4B, XL-5A and XL-5B).

## 4. Methods

Preliminary microtextural observations raised microbially mediated mineralization that is why adequate methods were chosen (Table S1). Mineral assemblage of such kind of systems is very fine grained and poorly crystallized, that is why very sensitive, high resolution, *in situ* methods were used with low excitation energy (FTIR, Raman spectroscopy). Also, they offer organic matter identification as well. Excitation energy of FTIR is the least, so it is the best for poorly crystallized microbially mediated minerals, even Raman with its higher excitation energy can cause transformation of minerals to more stable forms, e.g. ferrihydrite to goethite or hematite (Biondi et al. 2020). XRD is not adequate on such fine grained microbially mediated poorly crystallized samples, as they are XRD amorphous. So, to get information on mineralogy and organic matter, FTIR and Raman are the perfect methods.

### 4.1. Optical rock microscopy (OM)

Petrographic structural-textural studies were made on three thin sections (XL-4A, XL-5A, and XL-5B) in transmitted light (NIKON ECLIPSE 600 rock microscope, Institute for Geology and Geochemistry, Research Centre for Astronomy and Earth Sciences, - IGGR RCAES, Budapest, Hungary). In total 71 photos were taken. The samples do not show macroscopic lamination, that is why the thin sections were prepared on different orientations. Transmitted and reflected methods were used.

### 4.2. Cathodoluminescence (CL) observation

Cathodoluminescence (CL) was carried out on two thin sections (XL-5A, XL-5B) using a Reliotron cold cathode cathodoluminescence apparatus are mounted on a BX-43 Olympus polarization microscope. Accelerating voltage was 7–7.7 keV during the analysis. Cathodoluminescence spectra were recorded by using an Ocean Optics USB2000 + VIS-NIR spectrometer. Spectrometer specifications are 350–1000 nm wavelength range, and 1.5 nm (FWHM) optical resolution. 34 photos were taken.

### 4.3. Fourier transform infrared spectrometer (FTIR)

Fourier transform infrared (FTIR) was used for *in situ* micro-mineralogy and organic material identification on four thin sections, using a Bruker FTIR VERTEX 70 equipped with a Bruker HYPERION 2000 microscope with a 20 × ATR objective and MCT-A detector. During attenuated total reflectance Fourier transform infrared spectroscopy (ATR) analysis, the samples were contacted with a Ge crystal (0.5 μm) tip with 1 N pressure. The measurement was conducted for 32 s in the 600–4000 $cm^{-1}$ range with 4 $cm^{-1}$ resolution. Opus (version 5.5) software was used to evaluate the data. The equipment cannot be used for Mn-oxide determination because those peaks fall in the <600 $cm^{-1}$ range. Contamination by epoxy glue, glass was taken into consideration. Totally 139 FTIR spectra were taken at 16 parts in four thin sections, mineral phases in samples are summarized in Table S2.

### 4.4. Raman spectroscopy

High resolution *in situ* micro-Raman spectroscopy was used for micro-mineralogy and organic matter identification and distribution on 4 thin sections (XL-4A, XL-4B, XL-5A, XL-5B, line profiles are shown on Fig. 4). A Thermo Scientific DXR Raman Microscope was used, with a 532 nm (green) diode pumped solid-state (DPSS) Nd-YAG laser using 1.5 mW laser power, 50x objective lens in confocal mode (confocal aperture 25 μm slit). Acquisition time was 1 min and spectral resolution was ~2 $cm^{-1}$ at each measurement (Szeged University, Hungary); the distance between each point was 10 μm and the measurement time was 10 min. Diagrams were organized on peak height versus analytical spot number of each of the phases along the Raman scanned section. Intensities were normalized to the highest peak for each spectrum.

The spectra were elaborated in two ways:

(1) Diagrams were organized in terms of peak height versus analytical spot number of each of the phases along the Raman scanned section (intensity of main minerals and organic matter in general). (2) A detailed determination of all spectra was also made. These results are summarized in Table S3, in which the mineral composition can be followed from point to point, as well as the type of organic matter. Aside from the profile analyses, descriptions of the mineral phase transitions were also constructed for clarification of mineral transitions in three photos and two profiles.

The following Raman bands were used for normalization: rhodochrosite: ~1086 $cm^{-1}$, calcite: ~1083 $cm^{-1}$, kutnohorite: ~1093–96 $cm^{-1}$, apatite: ~965 $cm^{-1}$, quartz: ~463 $cm^{-1}$; carbonaceous matter: ~1605 $cm^{-1}$. Identification of minerals was made with the RRUFF Database (Database of Raman – spectroscopy, X-ray diffraction, and chemistry of minerals: http://rruff.info/), and cited papers given in Table S3. Contamination by epoxy glue was taken into consideration.

In total, 12,325 spectra were determined for micro-mineralogical and organic matter composition and also for the distribution of minerals and organic matter according to the thin section profiles. The pathways of analyzed profiles are shown in Fig. 4.

### 4.5. Major element analysis

Whole rock major elements analyses were carried out by the ALS Chemex Laboratory (Guangzhou, China) on five samples from the Xinglong section. Each whole-rock sample was crushed to 60 mesh in a corundum jaw crusher and then powdered in a tungsten carbide ring mill to finer than 200 mesh. Major-element measurements were made using a Shimadzu 1800X X-Ray fluorescence (XRF) unit with a detection limit of 0.1–1 ppm and an analytical precision better than ±3% of reported values. Loss-on-ignition (LOI) was used to determine total volatile content.

### 4.6. Electron probe micro-analyser (EPMA)

EPMA analyses include back scattered electron images, X-ray element maps, and also spectra with composition. Element composition and microtextural features of four thin sections (XL-4A, XL-4B, XL-5A, XL-5B) were determined at 1–2 μm spatial resolution on carbon-coated sample using a JEOL Superprobe 733 electron microprobe with an INCA Energy 200 Oxford Instrument Energy Dispersive Spectrometer, run at 20 keV acceleration voltage, 6 nA beam current and count time of 60 s for the spot measurement and 5 min for line-scan analysis. Olivine, albite, plagioclase and wollastonite standards were used; we estimated that the detection limit for the main elements was below 0.5% based on earlier measurements with various samples (IGGR RCAES, Budapest, Hungary). 355 spectra were acquired (element maps were also elaborated), and 24 back scattered electron images were made.

### 4.7. Stable C and O isotope study

$\delta^{13}C$ and $\delta^{18}O$ were measured on carbonates (whole rock samples) (rhodochrosite, kutnohorite, calcite, n = 2) and also on organic matter (n = 2) using a Finnigan Delta V continuous-flow mass spectrometer equipped with a Thermo Flash element analyser (IGG RCAES, Budapest,

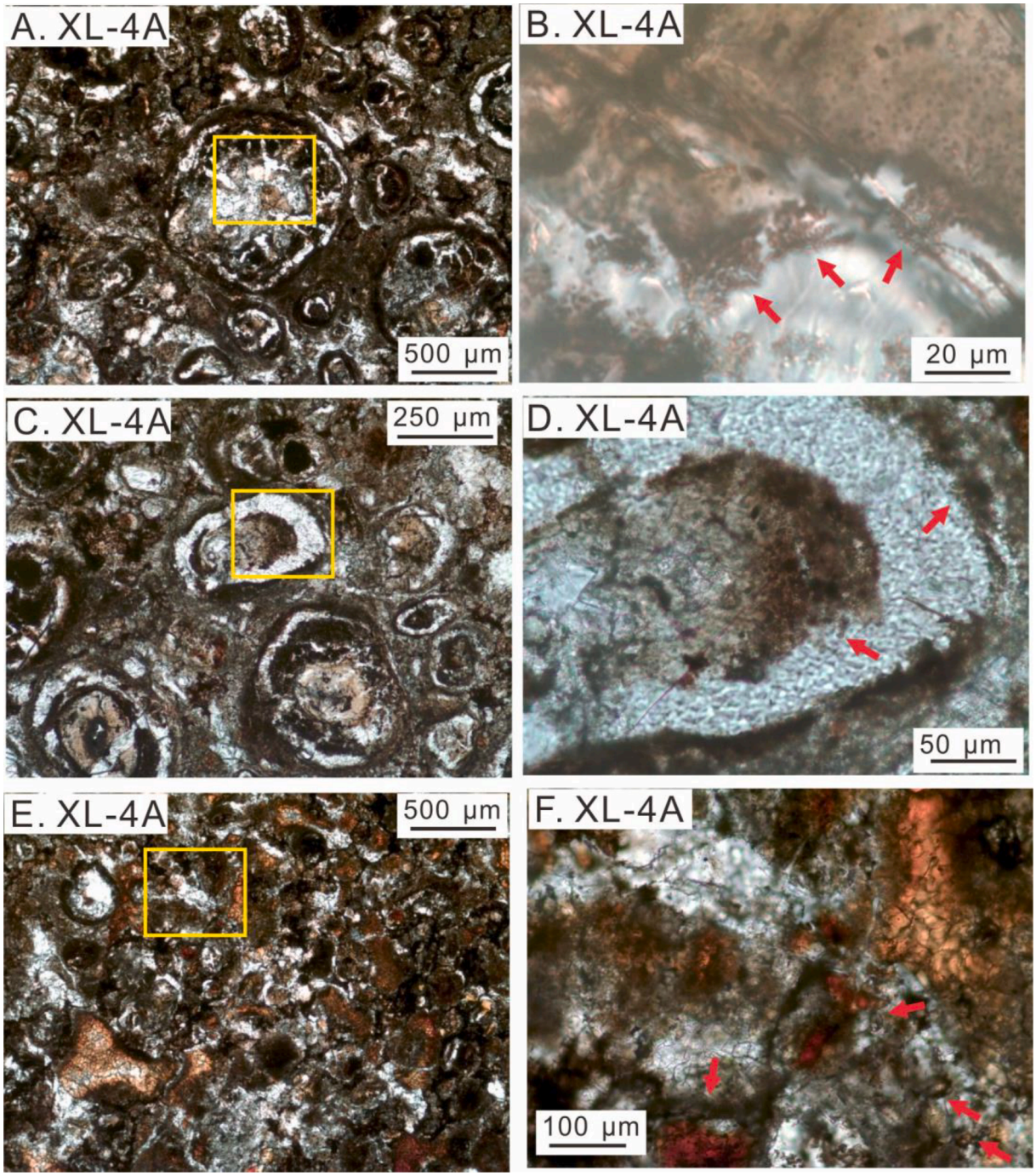


**Fig. 5.** The mineralized microbially produced micro-texture (MMPT) in thin section XL-4A. Panels A, C, E are showing the genal microscopical feature of this sample, with obvious nodules and grains floating in the micritic matrix. Panels B, D, F are zoom-in photos of the yellow rectangle in panels A. C. E, MMPTs are denoted by red arrows.

Hungary). Three sets of samples were measured for comparison. Results are given in per mil (‰) versus V-PDB ($^{13}C$) and SMOW ($^{18}O$) standards. Standard deviation of the data is below 0.1‰ based on the reproducibility of sample triplets and laboratory standard data. Measurements in case of carbonate were organic matter free and in case of organic matter carbonate free.

## 5. Result

### 5.1. Petrography

Sample XL-4A do not show macroscopic nor microscopic lamination. The sample is coarse-grained, diagenetically recrystallized. Debris material is not visible. Diagenetic sedimentary features can be observed (vein fillings), and coarse calcite mineralization was detected. Mineralized microbial and microfossil biosignatures are common (red arrows in Fig. 5 B D F). Mineralized microbial biosignatures occur as woven textures, filamentous forms with pearl necklace-like inner texture,

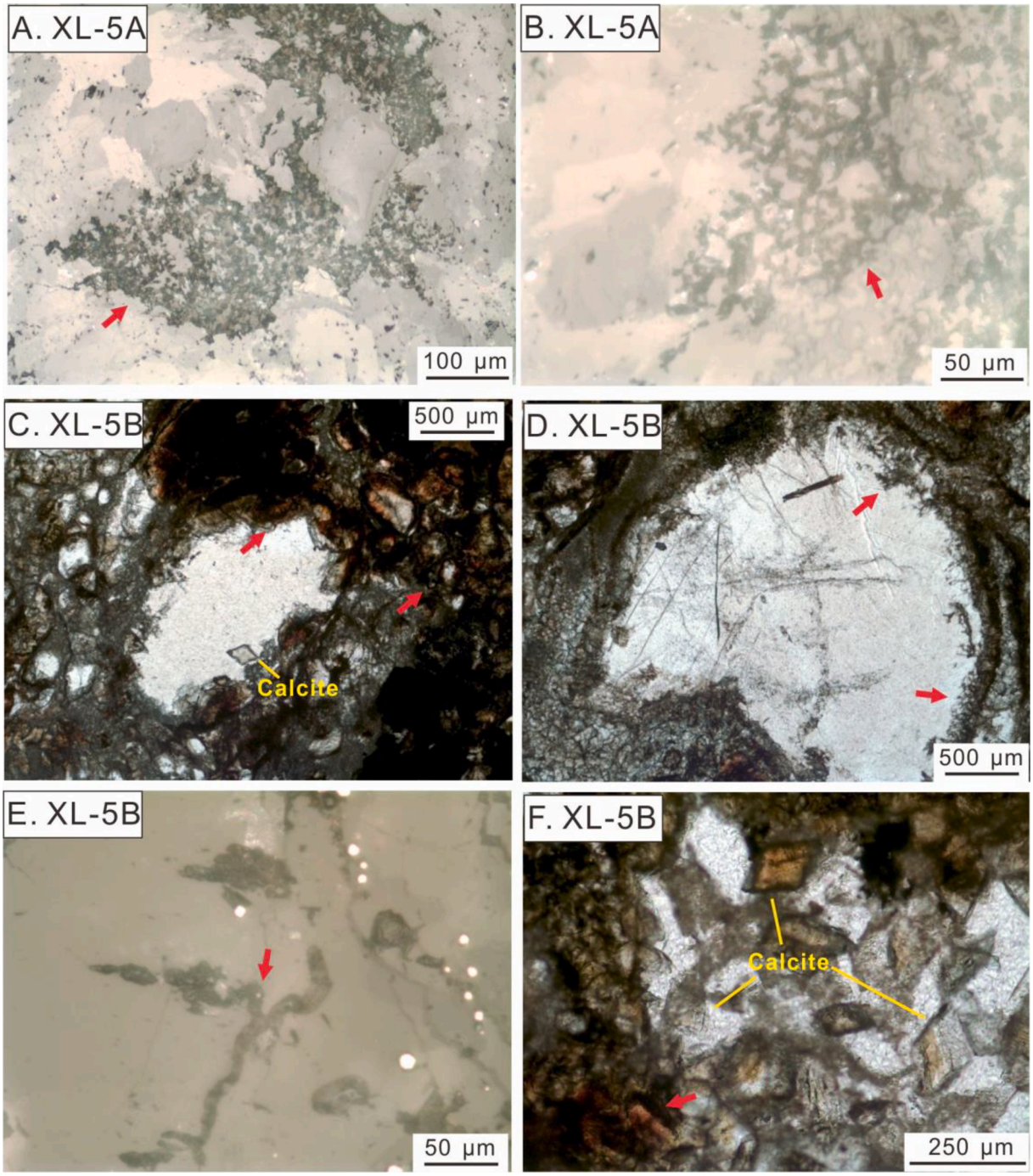


**Fig. 6.** The mineralized microbially produced micro-texture (MMPT) in thin section XL-5B. A and B are showing the mineralized microbial network (reflection light photos, red arrows). C and D are showing the MMPTs (red arrows, transmission light photos). E is presenting the tube-like structure, bright minerals are pyrite (reflection light photo). F automorphic calcite in micrometer scale.

vermiform and coccoid forms. Brownish Fe-bearing and organic-rich parts are very characteristic (Fig. 5). XL-5A and XL-5B samples similarly to XL-4A, do not show macroscopic nor microscopic lamination. In XL-5A sample very characteristic, representative mineralized microbial network can be observed on reflective photos (Fig. 6A B). Debris material is not visible. The samples are coarse-grained, diagenetically recrystallized. Brownish Fe-bearing and organic-rich parts can also be observed. In XL-5B sample, coarse calcite mineralization was detected (Fig. 6 C F). Mineralized microbial biosignatures are common (red arrows) (Fig. 6).

Microfacies of the manganese ore samples are wackestone and packstone. Abundant fossils are found within these samples, assembly of foraminifers (*Archaediscus* sp.), Echinoid spines, calcareous alga fragments, crinoid and Echinoderm plates and bryozoan indicate that manganese deposit was deposited in shallow warm sea water. Echinoid spines and *Archaediscus* sp. constrain the deposition age to Permian. Please see Fig. S1 for detailed information of micropaleontology.

### 5.2. Mineralogy

In microscopic photos, dark brownish obscure part occur in the manganese ore samples (Fig. 7A C E), which does not show CL, indicating organic matter and/or Fe-bearing minerals. Diagenetic carbonates show bright orange CL, indicating the feature of manganese carbonate minerals, e.g., rhodochrosite, Mn-bearing calcite, and kutnohorite (Fig. 7B D F). The small differences in CL can reflect

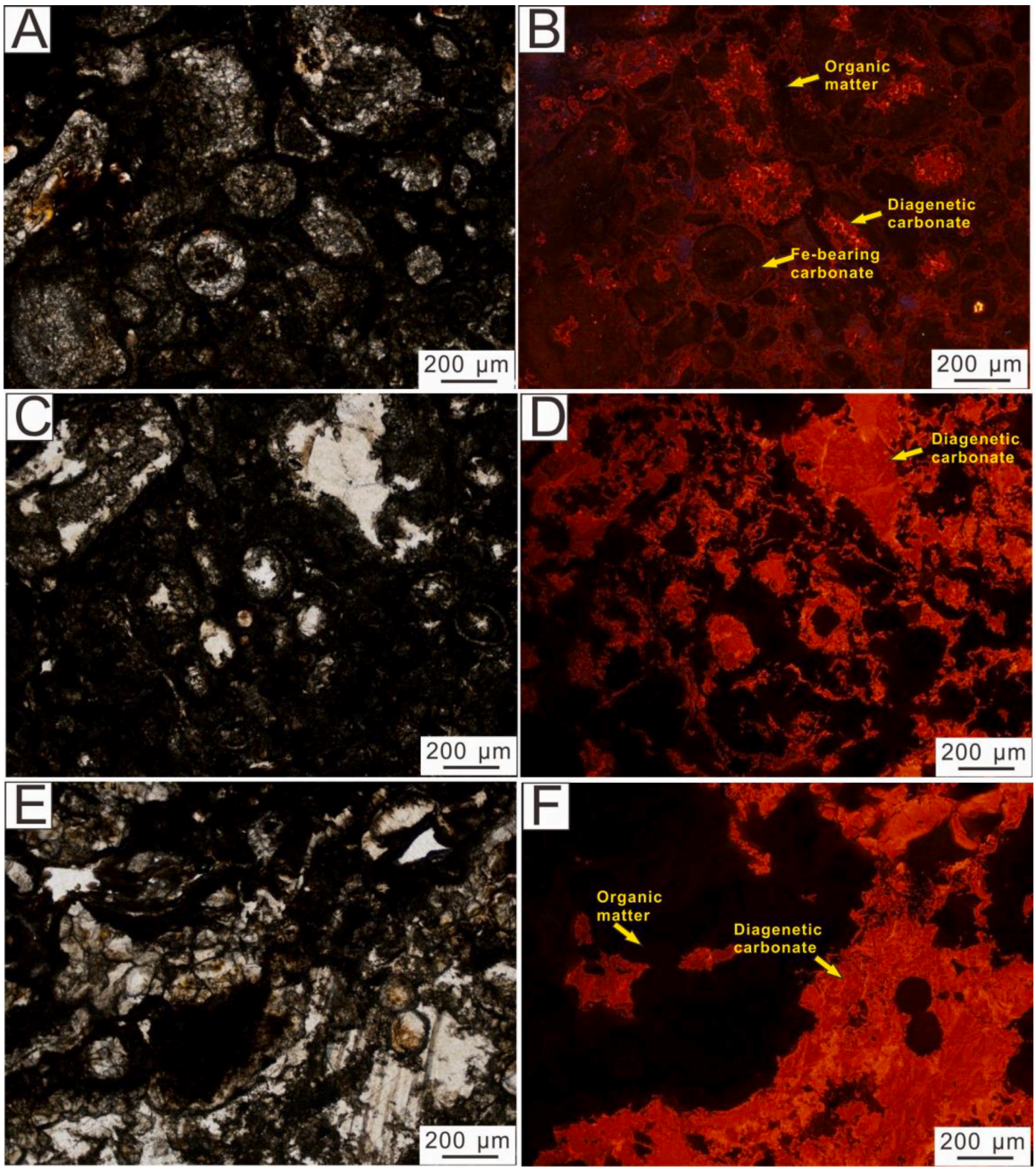


**Fig. 7.** Polarize microscope and cathodoluminescence (CL) photos of sample XL-4 (A, B, C, and D) and sample XL-5 (E and F), paired photos show the same view field of polarize microscope and CL photos. Bright orange phases are mixed carbonates, bluish phase on B is quartz.

transitional mineral phase of mixed carbonates. Dull orange CL can represent Mn-bearing carbonate affected by Fe-quenching. Blue CL parts (Fig. 7B) can represent segregated quartz. Debris component was not detected by CL.

From FTIR observations, the main Mn mineral is rhodochrosite, other manganese carbonates include kutnohorite and Mn-bearing calcite, siderite and dolomite also occurred (Fig. 8, Table S2). Fe oxide-hydroxide as ferrihydrite and hematite and locally pyrite was determined (Fig. 8C D E F). In mineralized microbial network, ferrihydrite, hematite, braunite, aegirine, albite and rhodochrosite occurred (Fig. 8C D). The organic matter is frequent. Besides ore minerals, apatite, feldspar (albite) and quartz were also detected.

According to the Raman spectroscopy, the main mineral distribution was evaluated visually based on series of Raman profiles using 10 μm scale (Fig. 9, Fig. S2–S5). Sample XL-4A, XL-4B and XL-5B show similar characteristic in the mineral distribution, mineral composition curves are dominated by Mn and Fe minerals' cycles (Table S3). Mn mineral assemblage includes: *Oxides and hydroxide*: pyrolusite, ramsdellite, jacobsite, todorokite, psilomelane, manjiorite, manganite, pyrophanite; *Carbonates:* rhodochrosite, kutnohorite, Mn-bearing calcite; *Oxides-silicates:* braunite, serandite; *Sulfides:* rambergite, alabandite. Fe mineral assemblage includes: *Oxides and hydroxides:* ferrihydrite, lepidocrocite, hematite, goethite, magnetite, anatase; *Carbonates:* siderite, ankerite; *Silicates:* nontronite, celadonite *Sulfides:* pyrite, marcasite. Other mineral assemblage includes: *Oxides and hydroxides:* quartz; *Silicates:* albite, mica, montmorillonite; *Phosphates:* apatite; *Sulfates:* Na-jarosite, johannite (uranyl sulphate). The mineralized Mn cycles are formed by alternating rhodochrosite and organic matter or kutnohorite and organic matter. Rhodochrosite and kutnohorite are occasionally overlapped, but tend to show independent peaks. The mineralized Fe cycle in sample XL-4 mainly consists of pyrite, it frequently formed cycles in the mineralogical curve (Fig. 9 and Fig. S2). Besides, quartz also show the cyclic feature. Sample XL-5A is a representative sample containing peculiar minerals (Fig. S3). Mn cycles and Fe cycles are both observed in this sample, the Mn cycles are represented by the mineral cycles of alternating rhodochrosite and organic matter or kutnohorite and organic matter, which are similar with the sample XL-4A and XL-4B. For mineralized Fe cycles, pyrite is the dominant Fe-bearing mineral phase, while marcasite ($FeS_2$, the polymorphic form of pyrite) and anatase [$(TiO_2)$ $Fe_xTi_{(1-x)}O_{(2-x)}OH_x$] are also observed in this sample. In the mineralogical curve, various Fe-bearing minerals show cyclic changes (Fig. S3 and Fig. S5): The Interval I (0 – 10,000 μm on Fig. S3-Distance/μm) contains only pyrite, the Interval II (10,000 – 25,000 μm) shows the mineral assembly of marcasite + quartz + pyrite + anatase, and the Interval III (25,000 – 30,700 μm) contains Fe-bearing minerals of anatase + pyrite.

### 5.3. Geochemistry

Five samples (XL-1 – XL-5) were acquired whole rock major elements results (Table 1), showing similar geochemical composition. Dominant element in these samples is MnO (24.01 wt% – 25.02 wt%). CaO (10.35 wt% – 13.60 wt%) and MgO (4.03 wt% – 5.51 wt%) are also high. $Al_2O_3$ (3.19 wt% – 6.00 wt%) and $SiO_2$ (5.64 wt% – 11.00 wt%) are relatively low, $TFe_2O_3$ and $TiO_2$ show moderate contents, ranging from 2.14 wt% to 2.39 wt% and 0.24 wt% to 0.65 wt%, respectively. $Na_2O$ (0.04 wt% – 0.09 wt%) and $K_2O$ (0.06 wt% – 0.08 wt%) are very low in Zunyi manganese ore samples. Total organic carbon (TOC) shows variations between 0.03 wt% and 0.26 wt%.

EMPA data support the results of other methods concerning mineralogy. The material is very fine-grained, so the analyses often give "mixed" composition. Some elements, like Ca, Mn, Mg and Fe, in carbonate minerals show highly variable composition. In total of 96 points give the valid geochemical composition results for different carbonate types, results were summarized in CaO-MnO-MgO triangle diagram (Fig. 10). The diagram indicates a transitional carbonate mineral series within the manganese ore samples, including calcite, Mn-bearing calcite, kutnohorite with variable composition (Ca-(Mn + Mg)), and rhodochrosite (Ca-, and Ca + Mg-bearing). Ion substitutions between $Ca^{2+}$, $Mg^{2+}$and $Mn^{2+}$ are common, according to the mineral phases.

Element distribution of samples is shown in Fig. 11. Fe occurs in different mineral phases: carbonates (siderite, mixed carbonate), oxide-hydroxide, sulfides (pyrite, marcasite), anatase (Fe-bearing), and clay minerals (celadonite, nontronite). Distribution of Ti and Fe show superposition in the biomat-like microtexture of some parts in thin sections, concentrated in the periphery of the Mn carbonate minerals (Fig. 11A C).

### 5.4. Stable C and O isotope results

Paired inorganic carbon isotope ($\delta^{13}C_{carb}$) and organic carbon isotope ($\delta^{13}C_{org}$) results in the manganese ore samples show similar composition (Table 1 and Fig. 12). Values of $\delta^{13}C_{carb}$ are low, ranging from −9.44‰ to −6.81‰, while $\delta^{13}C_{org}$ values are relatively high, ranging from −23.13‰ to −15.01‰. Oxygen isotope ($\delta^{18}O_{SMOW}$) values range from 25.50‰ to 26.10‰. Acquired carbon and oxygen isotope data are accordant with the published isotope data (Xu et al., 2019), which reported the $\delta^{13}C_{carb}$ values and $\delta^{18}O_{SMOW}$ values of the manganese ores range from −18.15‰ to −0.55‰ (average −7.78‰) and 21.64‰ to 26.07‰ (average 24.54‰), respectively.

## 6. Discussion

### 6.1. Microbial and mineralogical systems in the Permian manganese deposits of Zunyi

Based on new sedimentological and mineralogical evidences, microbial contribution in the studied manganese ore samples of the Permian Maokou Formation in Zunyi are showing as common features (Figs. 5 and 6). Besides, the mineral assembly and the variable organic matter contents in manganese ore samples indicate the microbially-mediated mechanism of the ore beds. These characteristics are similar to the reported cases dominated by the microbially-mediated metallogenesis (Polgári et al., 2012b; Biondi and Lopez, 2017; Yu et al., 2019b; Biondi et al., 2020). Thus, we argue the manganese-rich deposits of the Permian Maokou Formation in Zunyi occurred as microbialites. Two microbial ore-forming systems are during the fixation of the manganese oxides, including the Fe-oxidizing metabolic process (Fe-oxidizing microbes) and Mn-oxidizing metabolic process (Mn-oxidizing microbes). Intense cyanobacterial activities also happened in this process, reflecting by abundant low- or non-manganese carbonate within the manganese ores. According to Castanier et al. (1999), the carbonate particles are produced by ionic exchanges through the cell membrane by autotrophy, which is non-methylotrophic methanogenesis and cyanobacterial photosynthesis. Carbonatogenesis is the response of heterotrophic bacterial communities to an enrichment of the milieu in organic matter. After a phase of latency, there is an exponential increase of bacterial numbers together with the accumulation of metabolic end-products deriving a pH increase and an accumulation of carbonate and hydrogen-carbonate ions (Dupraz and Visscher, 2005; Dupraz et al., 2009). Mn- and Fe-replacement via early diagenesis influence the calcite composition.

#### 6.1.1. Manganese systems

*6.1.1.1. Syngenetic manganese system.* The syngenetic manganese minerals (e.g., Mn-oxides, Mn-hydroxides) are usually hard to preserve in the ancient manganese carbonate deposits. They could easily transform to carbonate minerals during the early diagenesis (Burke and Kemp, 2002; Johnson et al., 2016b). In this study, a small quantity of Mn-oxides and Mn-hydroxides minerals such as todorokite and manganite along

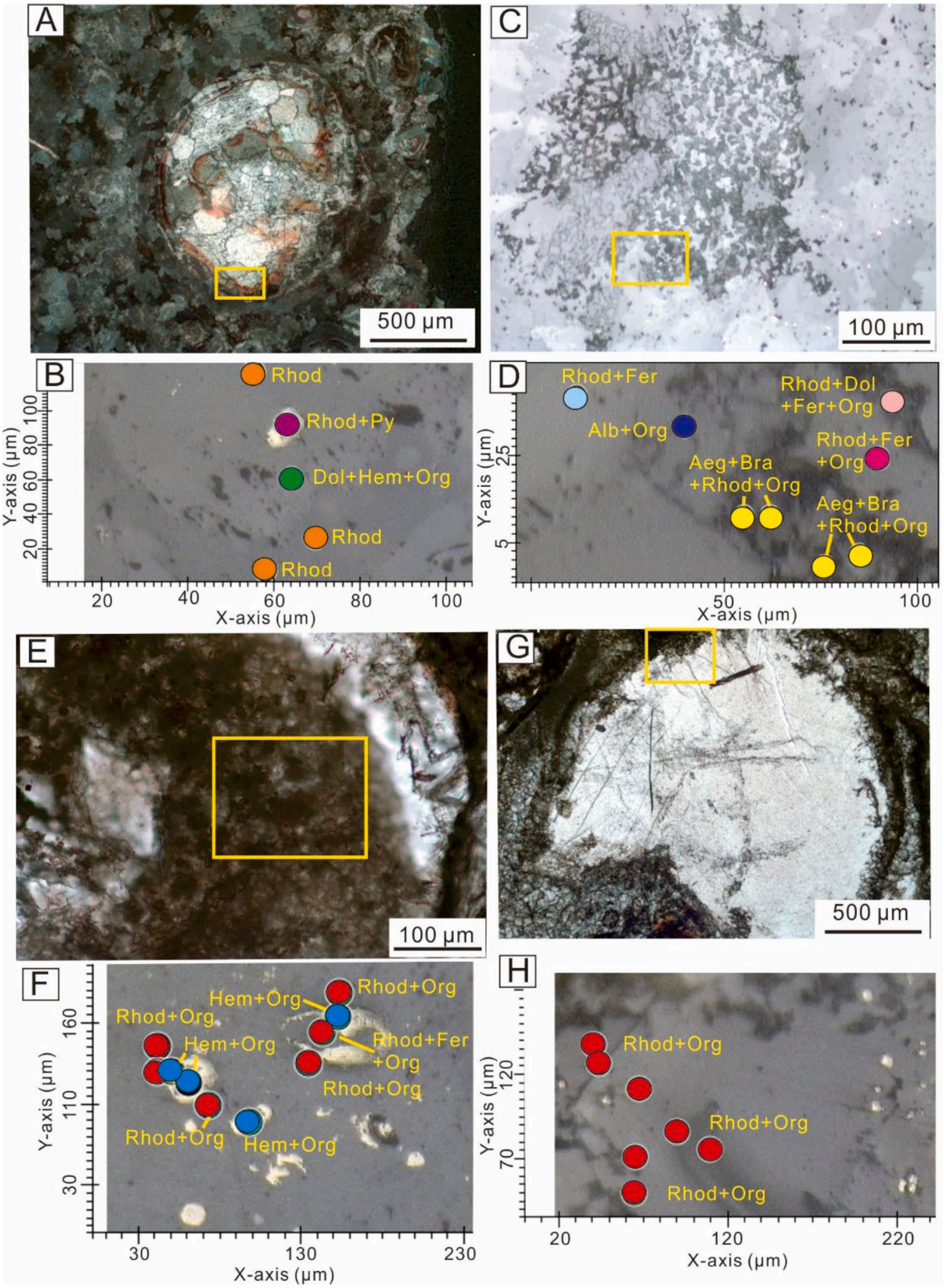


**Fig. 8.** Optical observation (upper) and analyzed points of Fourier transform infrared (FTIR) spectrometer (lower) in sample XL-4 (A and B) and XL-5 (C, D, E, F, G and H), yellow rectangles in optical photos show the same field of view in FTIR photos, colored dots in FTIR photos indicate the analyzed points. Please see results in supplementary materials. For abbreviation: Rhod- rhodochrosite; Py-pyrite; Dol-dolomite; Hem-hematite; Fer- ferrihydrite; Aeg-aegirine; Bra- braunite; Alb- albite; Org-organic matter. Different colors in analyses dots indicate various mineral/mineral assembly.

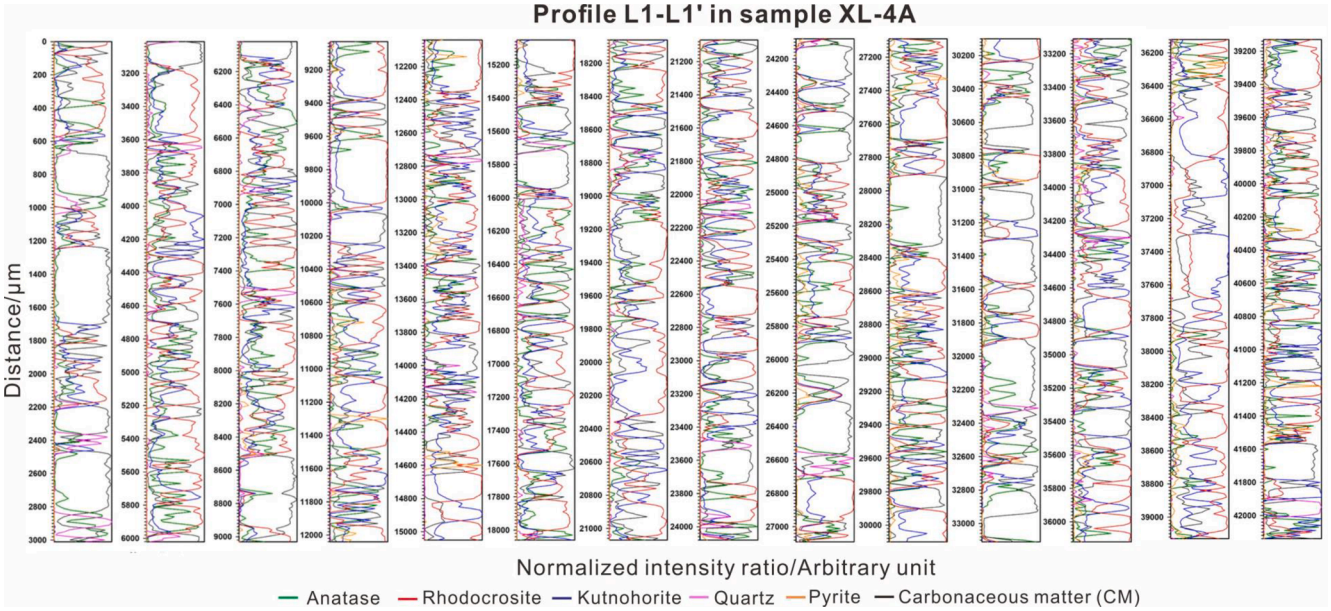


**Fig. 9.** Mineralogical and organic matter distribution in the Raman profile of sample XL-4A (scan path is along L1-L1′ in Fig. 4A).

with hydrocarbons were identified by the Raman and FTIR analyses (Table S2 and Table S3). We consider them as remnants of the original sedimentation, for these syngenetic minerals were not entirely destroyed during diagenesis. Precipitation of Mn-oxide and Mn-hydroxides formed the protore of manganese deposit in the Maokou Formation, the initial product of microbial enzymatic Mn(II) oxidation may lead to the formation of bio-oxides/ hydroxides (e.g., todorokite, manganite), similar to the modern microbial simulation experiments (Bargar et al., 2005; Vandieken et al., 2012). The microbial (enzymatic) Mn(II) oxidation requires obligatory oxic condition, this bio-oxide is an amorphous oxide similar to δ-$MnO_2$ (as todorokite and manganite detected by Raman in XL-4 and XL-5 samples, Table S3), which is thought to be a disordered thermodynamically unstable 7-Å-vernadite (hexagonal phyllomanganate) containing Mn(IV) vacancy defects, with very small particle sizes (<20 nm lateral dimensions), and having only two or three $MnO_2$ layers stacked along the c-axis (Villalobos et al., 2003). The bacterial cells not only directly oxidized Mn(II) to Mn(IV), but also influenced the cation composition of the Mn-oxide mineral being produced during the early stages of Mn oxidation process (Bodeï et al., 2007). Mineralogical changes similar to these are commonplace in natural settings where bacterial oxidation of Mn(II) occurs and may liberate absorbed metal ions or alter the rates of Mn-oxide surface processes, such as the degradation of organic matters. It is noteworthy that microbes may exploit such mineral transformation reactions to indirectly control chemical conditions in the vicinity of the cell (Mandernack et al., 1995). Other two possible pathways for formation of mixed carbonate mineral phases include Mn-metasomatism of calcite (Molnár et al., 2017) and primary rhodochrosite precipitation (Wittkop et al., 2020). The former is accomplished by the process that the $Mn^{2+}$ ions in water replace the $Ca^{2+}$ of the calcite produced by cyanobacteria and resulting in the formation of Mn-bearing calcite; the latter is an innovative mechanism that believes primary Mn-carbonates are precipitated in environments with high concentrations of dissolved Mn (>200 μM), and where Fe and Mn are partitioned by S cycling, photoferrotrophy, or microaerophilic Fe-oxidation.

*6.1.1.2. Diagenetic manganese system.* Rhodochrosite and kutnohorite are considered as diagenetic products forming the main Mn ore. Composition of kutnohorite reflects Ca – (Mn + Mg) cation composition, existence of Mn-bearing calcite within the samples indicate the possible process of Mn-metasomatism (Fig. 10). Mn-bearing carbonate phases in the samples show transitional geochemical compositions. In the diagenesis, the syngenetic Mn-oxide/hydroxides stabilized and formed relatively pure mineral phases (such as pyrolusite, ramsdellite, Table S3) and/or variable-cation-bound forms such as pyrophanite, romanèchite, manjiorite and jacobsite (Polgári et al. 2012ab; Maynard, 2014; Johnson et al., 2016b; Biondi et al., 2020). Activities of heterotrophic microbes during the early diagenesis led to the precipitation of rhodochrosite.

$\delta^{13}C_{carb}$ values of samples are moderately negative, between −9.44‰ to −6.81‰. Concerning carbonate formation three models can be discussed: (1) Abiogenic mixed syngenetic carbonate formation (heavy C signal); (2) Cyanobacterially mediated syngenetic calcite formation and Mn- and Fe-replacement via early diagenesis (both C isotope signals can occur), and (3) Diagenetic mixed carbonate formation via organic matter decomposition (light C signal). Measured values will be the resultant of the different C sources, which moderate negative character refer the major contribution of heavy C source. Microtextural features of samples clearly show that sediment surface was colonized by cyanobacteria. Carbon isotope data of the Permian manganese and carbonate deposits in Zunyi give the direct evidence for the reaction between syngenetic Mn-oxide/hydroxides and organic matter (Fig. 12), the inorganic carbon isotope records in the manganese ore samples (−17‰ to ~−5‰) are much lower than non-manganese carbonate (0.5‰ to 5‰), indicating that the carbon source partly originate from the oxidized organic matter (Xu et al., 2019 and this study). This observation is widely existed in the manganese carbonate deposits in different ages around the world (Polgári et al., 1991; Yu et al., 2017). These poorly mineralized cryptocrystalline minerals mixed in a variable amount of the micro-laminae as a manifestation of mineralized manganese cycles. Manganese sulfide (MnS) minerals (ramsbergite and alabandite) are observed in both XL-4 and XL-5 samples, they usually coexist with kutnohorite. Appearance of MnS minerals indicate that the manganese-rich sediments once reaching the depth of sulfate reduction zone (SRZ) with excess of organic matter, which is accordant to the observation of microbial involved mineral synthesis experiment and modern marine sediments in Baltic sea (Burke and Kemp, 2002).

*6.1.2. Iron systems*

*6.1.2.1. Syngenetic iron system.* Fe-oxides (hematite) and Fe-hydroxides (ferrihydrite and lepidocrocite) in the samples represent the remnant of syngenetic Fe-bearing minerals (Fig. 8 and Table S2). Considering the

**Table 1**
Compositions of major elements, organic carbon, C and O isotopes for Middle Permian Mn ore samples in Zunyi, South China.

| Sample | $SiO_2$ wt.% | $Al_2O_3$ wt.% | $TFe_2O_3$ wt.% | MnO wt.% | MgO wt.% | CaO wt.% | $Na_2O$ wt.% | $K_2O$ wt.% | $TiO_2$ wt.% | $P_2O_5$ wt.% | BaO wt.% | $SO_3$ wt.% | LOI 1000 wt.% | SUM wt.% | C organic wt.% | $\delta^{13}$Ccarb VPDB, ‰ | $\delta^{13}$Corg VPDB, ‰ | $\delta^{18}$O VSMOW, ‰ |
|---|---|---|---|---|---|---|---|---|---|---|---|---|---|---|---|---|---|---|
| XL-1 | 5.64 | 3.19 | 2.39 | 24.47 | 5.51 | 13.60 | 0.04 | 0.06 | 0.24 | 0.01 | 0.02 | 1.90 | 42.64 | 99.71 | 0.03 | −7.13 | −21.23 | 26.10 |
| XL-2 | 10.75 | 4.79 | 2.38 | 25.02 | 4.03 | 10.35 | 0.05 | 0.07 | 0.54 | 0.01 | 0.01 | 0.61 | 41.18 | 99.79 | 0.16 | −8.54 | −22.45 | 25.70 |
| XL-3 | 10.48 | 5.42 | 2.34 | 24.01 | 4.26 | 11.15 | 0.07 | 0.08 | 0.60 | 0.01 | 0.01 | 0.61 | 40.42 | 99.46 | 0.26 | −6.81 | −23.13 | 25.50 |
| XL-4 | 10.04 | 5.11 | 2.26 | 24.24 | 4.37 | 11.30 | 0.09 | 0.08 | 0.65 | 0.01 | 0.02 | 0.69 | 40.35 | 99.21 | 0.20 | −7.40 | −22.11 | 25.60 |
| XL-5 | 11.00 | 6.00 | 2.14 | 24.16 | 4.04 | 10.45 | 0.07 | 0.08 | 0.65 | 0.01 | 0.01 | 0.55 | 40.04 | 99.20 | 0.21 | −9.44 | −15.01 | 25.60 |

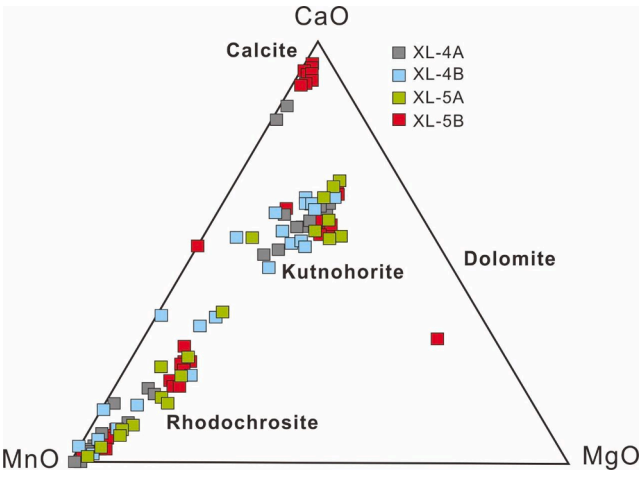


**Fig. 10.** CaO-MnO-MgO triangle diagram for the EPMA - EDS analyses of samples XL-4A, XL-4B, XL-5A and XL-5B.

Permian manganese deposits in Zunyi formed in the weakly oxidizing to reducing condition environments (Gao et al., 2018), several possible ferrous-oxidizing mechanisms can be proposed to explain the precipitation of Fe-bearing minerals: (1) Microbial neutrophilic, micro-aerobic Fe(II) oxidizing bacteria in weak alkaline and suboxic environment (Hallbeck and Pedersen, 1990; Ehrenreich and Widdel, 1994; Konhauser, 1998; Ehrlich, 2002); (2) Nitrate-reducing Fe(II) oxidizers in suboxic/anaerobic conditions (Straub et al., 1996); and (3) Photoferrotroph metabolism in anoxic/anaerobic light-demanding conditions (Konhauser, 1998; Konhauser et al., 2017).

## 7. Diagenetic iron system

Microbial poorly-ordered Fe-bearing minerals (e.g., ferrihydrite and lepidocrocite) in the Fe-rich biomat would transformed into more ordered and stable minerals, such as goethite, hematite and anatase (a $Fe^{3+}$ $Ti^{4+}$-bearing oxide), which have been observed in the Raman spectra (Table S3). In XL-4 and XL-5 samples, the anatase cycles are well established (Figs. 9, 13, Fig. S2, S3, S4 and S5). EPMA measurements determined Fe-content in the anatase in mineralized biomat-like microtexture (Fig. 11). Occurrence of siderite and ankerite within samples may indicate that sediments had reached the Fe reduction zone (FeZR, suboxic diagenetic zone). Aegirine is a trace mineral in XL-5A. Previous study of the end-Neoproterozoic manganese deposit in Urucum, Brazil reported this mineral as the main component of the manganese ores. Aegirine, as a more stable Fe-bearing mineral phase, occurring in cyclic micro-laminae alternating with braunite in Urucum, it is the diagenetic mineral formed by Fe-oxidizing bacteria (Biondi et al., 2020). The syngenetic Fe-oxides and Fe-hydroxides (ferrihydrite) transformed to aegirine and segregated silica during early diagenesis (Herdianita et al., 2000). Aegirine micro-laminae represent the Fe-oxidizing microbial cycles, and braunite represents the Mn cycle in silicified and stable form (Johnson et al., 2016a). This aegirine and braunite assembly should form in oxic-suboxic condition (Baturin, 1988). High-resolution Raman investigations show that aegirine consumes silica in hematitic biomat toward the silica fixation (Biondi et al., 2020). In short, the reported authigenic formation of aegirine fits well with our results, the source of Na was more likely came from the decomposition of cell and sequestered element in extracellular polymeric substances (EPS) or/and the hydrothermal activities.

Marcasite ($FeS_2$) is a peculiar mineral in XL-5A, which has an important role in the interpretation of diagenetic conditions (Table S4 and Fig. S5). Marcasite occurs together with the mineral assembly of quartz + pyrite + anatase in the sample (Table S4 and Fig. S5). As marcasite occurs in the form of cycles, it supports that this mineral

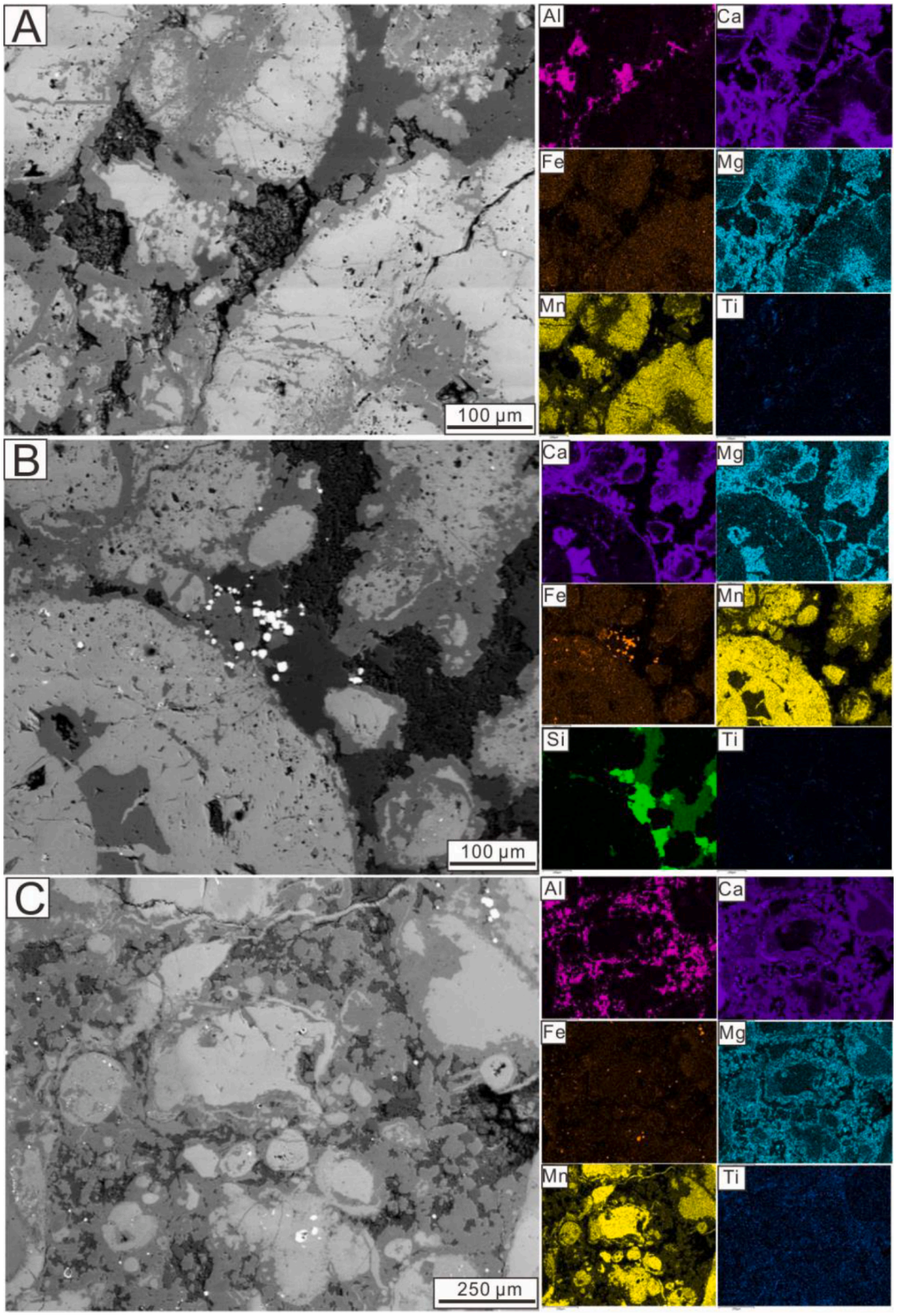


**Fig. 11.** EPMA back-scattered images (left) and EDS elements scanning images (right) of A, B sample XL-4 and C-sample XL-5. Analyzed elements included Ca, Mg, Fe, Mn, Si, Al and Ti. Ca, Mg, Fe, Mn represent mixed carbonate phases, on B white Fe enrichment is pyrite, Ti represent anatase, Al represent clay minerals, Si on B represent quartz (strong green part) and probably clay minerals (light green part). For more results please see supplementary materials.

represents the diagenetic product of Fe-biomat, which marcasite formed under special diagenetic conditions. Precipitation of marcasite needs an acidic environment, however, there is a sufficient number of diagenetic marcasite are found from normal marine sediments (Böttcher, 2011; Schieber, 2011), as well examples of marcasite that has inverted to pyrite (Schieber, 2011), suggesting that it might be widespread in the marine realm than previously thought. Formation of pyrite occurs in the condition of pH = ~6, but the formation of marcasite demands pH < 5. Thus, the relative abundance of pyrite versus marcasite in sediments should be a function of pH. Because marine waters are slightly alkaline

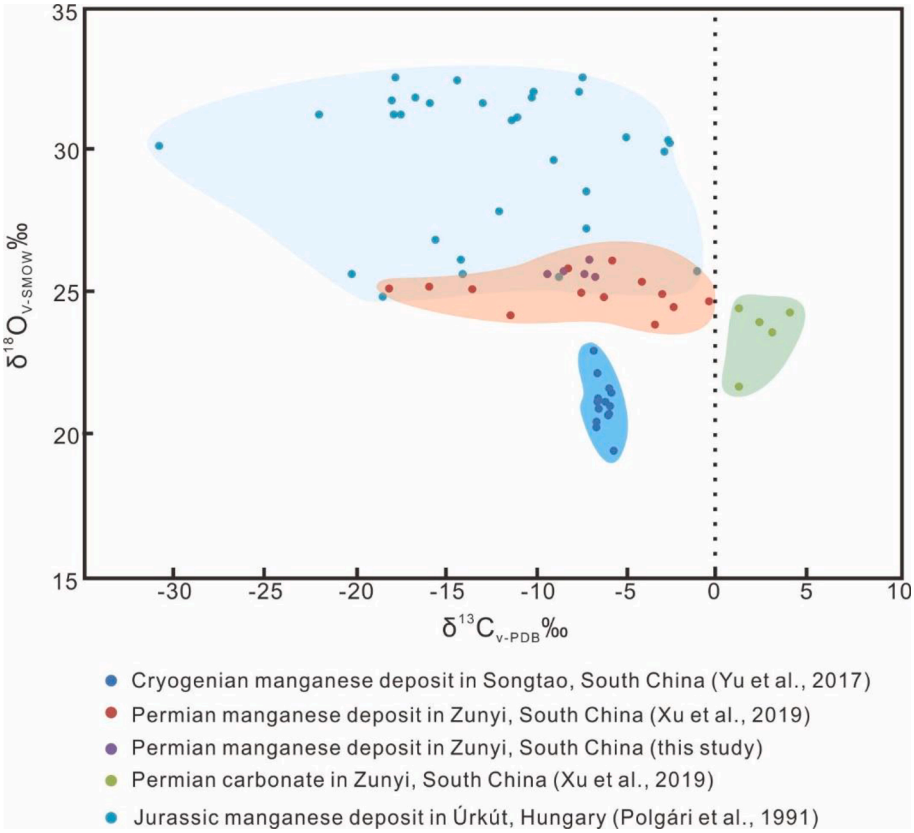


**Fig. 12.** Carbon and oxygen isotope data from the Permian manganese deposit in the Maokou Formation of Zunyi, northern Guizhou, South China (Xu et al., 2019 and this study), Cryogenian manganese deposit in the Datangpo Formation of Songtao, eastern Guizhou, South China (Yu et al., 2017), Jurassic manganese deposit in Úrkút, Hungary (Polgári et al., 1991).

(pH = ~8), it has been presumed that marcasite cannot form in marine sediments during the early diagenesis. Yet, regardless of this, diagenetic marcasite unquestionably occurs in marine sediments (Maynard, 1983). During the early diagenesis, pre-existing sulfide grains are wholly or partially destroyed, in order to supply dissolved $Fe^{2+}$, or readily soluble iron [e.g., $Fe(OH)_3$] for the growth of new iron sulfides. Iron sulfide destruction to sulfate results in acidity ($SO_4^{2-} + H^+$) and dissolved ferrous ion ($Fe^{2+}$). The associated lowering pH in the pore water also promotes larger concentration of $Fe^{2+}$ (Maynard, 1983). Such a setting favors re-precipitation of marcasite in the presence of $H_2S$ influx from underlying sediments (Murowchick and Barnes, 1986; Schoonen and Barnes, 1991). Re-oxidation of reducing, organic and iron sulfide-rich sediments ("burndown") has been studied extensively (Egger et al., 2017), and marcasite can potentially be used as a mineral based indicator of burndown events. Marcasite as a common component, occurs intimately associated with calcite dissolution and precipitation of diagenetic quartz. This mineralogical triumvirate makes chemical sense because marcasite formation, calcite dissolves and dissolved silica (segregated silica) precipitates all require low pH conditions. Amorphous silica segregation is derived by either the destruction of opaline components, organic complexes or the transformation of ferrihydrite (Baele et al., 2008).

### 7.1. Combination of hydrothermal and microbial metallogenic mechanism

Published studies on the Permian manganese deposits in the Maokou Formation of Zunyi emphasize the significance of the hydrothermal activities during the metallogenesis (Liu et al., 2008, 2015; Gao et al., 2018; Xu et al., 2019). Several reasons are proposed to explain the hydrothermal fluids facilitate the formation of manganese deposits: (1) hydrothermal vents at the bottom of the basin provided sources of Mn and Fe influxes for the seawater; (2) injection of hydrothermal fluids into the seawater probably led to the stratification of the basin waterbody and formed the oxic surface water and anoxic bottom water; and (3) hydrothermal activities led to the enrichment of REEs in manganese ores. These studies mentioned the biogenic factor that limited to enhance primary productivity and anoxic waterbody caused the increased organic carbon burial, which participated in the formation of manganese carbonates. However, based on new evidences of this study, we proposed that biogenic factor may play an important role during the manganese metallogenesis than previously thought.

Based on our results, an innovative metallogenesis mechanism involving both hydrothermal and geobiological processes is proposed to explain the formation of manganese deposit of the Maokou Formation in Zunyi. Basal seawater probably contained high content of Mn(II) which was supplied by distal hydrothermal fluids during the rifting activities at that time (Fig. 14A). Initial fixation of manganese should happen near the redoxcline of the basin, that is why the manganese deposits of the basin concentrated in the slope or the deep shelf margin environments (Liu et al., 2019), neither in the center of the basin nor in the platforms, the former is dominated with thin-layer siliceous rock and latter is pure limestone. The first step of the microbially-mediated manganese enrichment began with two important mechanisms in the oxic condition: (1) Enzymatic Mn(II) oxidation resulted in the precipitation of δ-$MnO_2$ bio-oxide (todorokite, manganite) as very fine-grained ooze into the cyanobacterial organic and carbonate network; (2) Metals were sequestered in extracellular polymeric substance (EPS) and other organic materials including carboxyl, sulphinic acid, phosphate groups, anions on amino groups. These processes sequestered dissolved Mn(II) into solid phase.

During the manganese enrichment stage, microbial mats were jointly organized by at least three types of microbial systems, including the (1)

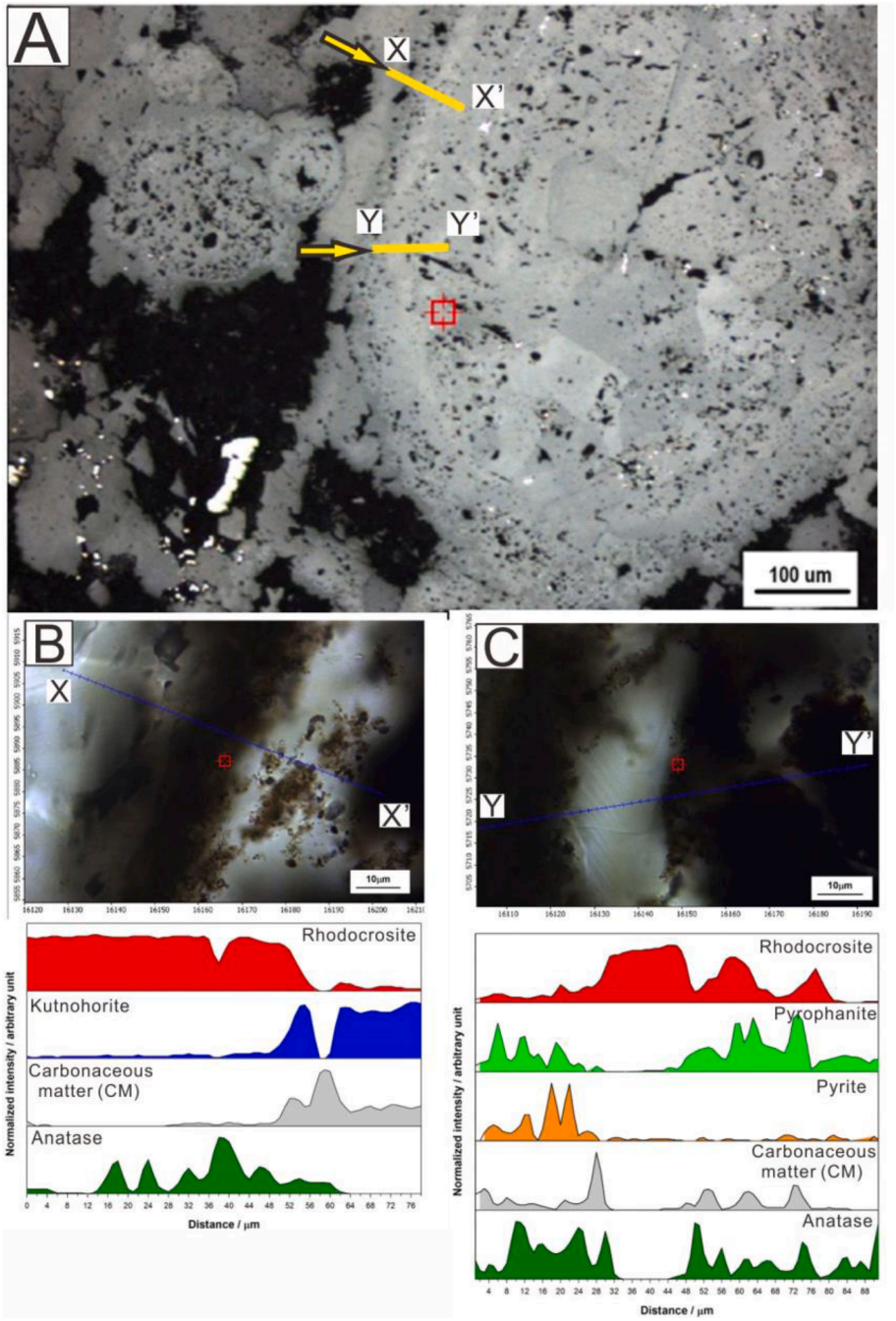


**Fig. 13.** Reflected optical rock microscopy image (A) and Raman scanning results (B and C) of mineralogical distribution of a nodule in sample XL-4A, arrows in Fig. 13A indicate the moving direction (photos on B and C are optical rock microscopy images, transmitted light, 1 N).

cyanobacterial system, (2) Mn-biomat system and (3) Fe-biomat system. Intense carbonate formation by cyanobacterial activities can be demonstrated by the widespread calcites, and they were partially affected by Mn-metasomatism and formed Mn-bearing calcite (Fig. 14B). It is interesting to observe peaks of Mn-bearing calcite/ rhodochrosite and kutnohorite show no overlapping (Fig. 11, Fig. S2, Fig. S3 and Fig. S4). Thus, we explain that Mn-bearing calcite/ rhodochrosite represent one system, indicating the co-existence of cyanobacteria and Mn-biomat (Fig. 14C). The kutnohorite cycles represent a more diagenetic level between direct carbonate formations (autotrophy) or heterotrophic cycles between autotrophic ones in the pause of autotrophic carbonate formation. Cyclic anatase in manganese carbonate ores of Zunyi is proposed as fossil Fe-biomat system. Similar anatase cycles have been observed in the Early Carboniferous manganese deposits in the central Guangxi, South China (Yu et al., 2021 current volume). Anatase biosignatures are reported as peculiar unique ones in impact suffered hydrothermal locality (Glamoclija et al., 2009), but our finding fits well with their proposed mineralized biosignature. Ti is bound on organic matter, and via decomposition and release of cations occurred, and in the ample of $Fe^{3+}$ the Eh-pH conditions under low temperature realized in the form of anatase crystal structure. The Fe content of anatase is not documented in that paper, but EPMA and Raman analyses detected that Fe exists together with Ti in mineralized biomat-like microtexture (Fig. 11 and Fig. 13). Based on these, the anatase cycles can be interpreted as the diagenetic product of Fe-biomat system. Pyrite in the mineral assemblage refers to anoxic, acidic conditions which could be favorable for Fe-bearing anatase mineralization.

After burial, cyanobacterial, Mn-biomat and Fe-biomat systems were

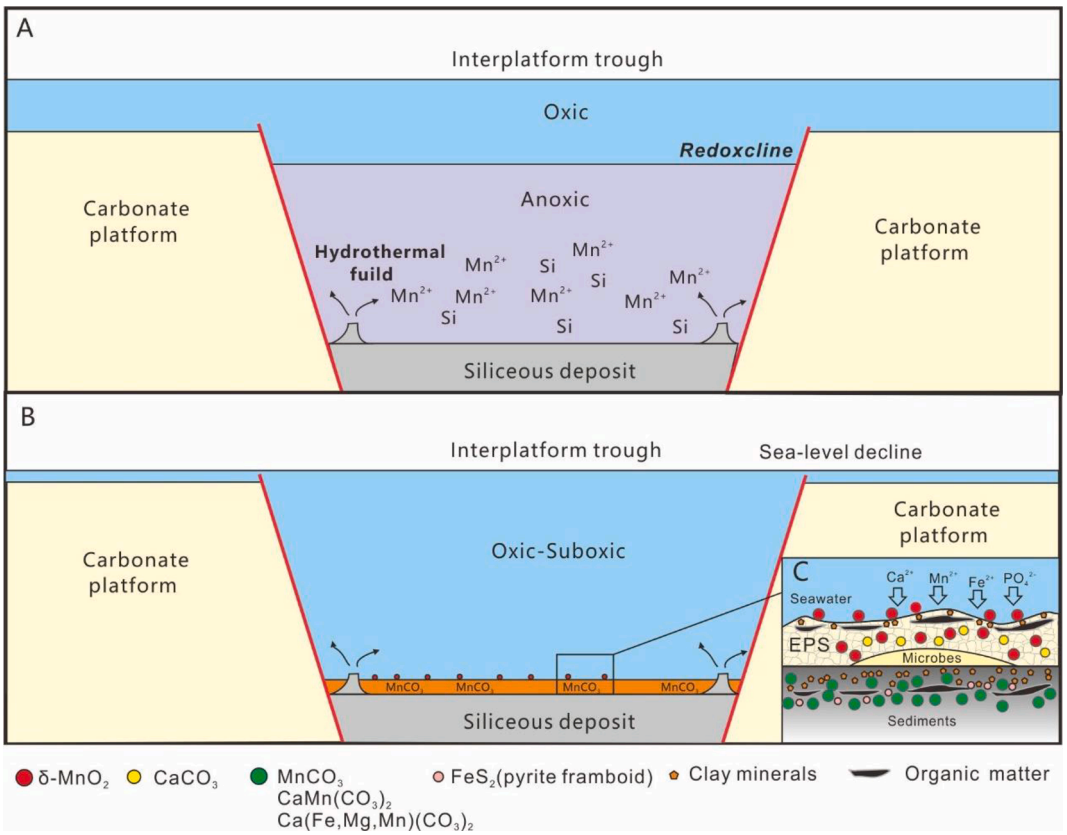


**Fig. 14.** Metallogenic model for the Permian manganese deposit in Zunyi, northern Guizhou. A-In the rifting stage, rapid submerge led to the deep interplatform trough, the hydrothermal source $Mn^{2+}$ accumulated in the anoxic deep watermass in the basin. B-After rifting stage, the doming effect of the ELIP (Emeishan Large Igneous Province) led to the regional uplift, which lead to the expansion of the oxic layer in the basin; C-Microbial activities led to the precipitation of Mn-oxides and then transformed to the Mn carbonate deposit. EPS = Extracellular Polymeric Substances.

combined. Considering the deposition depth was around the redoxcline, the redox conditions could range from suboxic to anoxic, at this contact zone between oxic/suboxic and anoxic conditions, a re-oxidation process occurred and resulted in cyclic marcasite within sample XL-5A. Ramsbergite and alabandite formation can be explained by the Mn sulfide – kutnohorite formation model established by Burke and Kemp (2002). Mn-sulfide crystals grew after deposition of a Mn-oxide lamina. The precipitation of Mn-sulfide in preference to Mn-carbonate requires a high excess of free sulfide relative to alkalinity and an environment completely depleted in Fe, otherwise Fe-sulfides would precipitate. High *in situ* $H_2S$ and alkalinity concentrations should be present below the Mn-oxide lamina. Large amounts of $Mn^{2+}$ can be produced rapidly by bacterial Mn reduction (and possibly by direct chemical reduction) of the Mn-oxide lamina, this provides a favorable environment for the formation of Mn sulfide and kutnohorite. For cyanobacterial and Mn-biomat systems, their behaviors during the early diagenesis have been discussed in detail in previous studies of the ancient microbially-mediated manganese deposits (Polgári et al., 2012b, 2019; Biondi and Lopez, 2017; Yu et al., 2019b; Biondi et al., 2020). Bio-oxide ($\delta$-$MnO_2$) reacted with the organic matter in the sediment through the microbially mediated processes and the Mn-metasomatism of the cyanobacterial carbonate jointly composing the main process during the formation of early diagenetic manganese carbonate ore, left the negative carbon isotope features of the manganese ores (e.g., $\delta^{13}C_{carb}$ of −9.44‰ to −6.81‰ in Zunyi manganese ores, Fig. 12). Thus, the combination of hydrothermal and microbial processes contributed to the formation of the Middle Permian manganese deposits in Zunyi.

## 8. Conclusions

Based on new sedimentary, mineralogical, and isotope evidences acquired from this study, we proposed that microbially-mediated metallogenic mechanism made the important contribution for the formation of the Middle Permian manganese deposits in the second Member of the Maokou Formation in Zunyi, South China. Manganese ores in Zunyi on macroscopic level show massive, clastic structures. Samples in thin sections are coarse grained, diagenetically recrystallized with abundant mineralized microbial and microfossil biosignatures. High resolution mineralogical investigations provided micrometer-scale cyclic occurrence of minerals and organic matter, as robust evidence of microbial contribution. Microbial and mineralogical systems in the manganese deposits could be subdivided into three categories: (1) cyanobacterial system, (2) Mn-biomat system and (3) Fe-biomat system. During the manganese metallogenesis, hydrothermal activities at the bottom of basin provided sufficient dissolved $Mn^{2+}$ ions into the anoxic basal waterbody. Near the redoxcline, cyanobacterial activities led to the precipitation of calcites, and they could be partially affected by Mn-metasomatism and formed Mn-bearing calcite, Mn-oxidizing microbes led to the precipitation of manganese bio-oxide ($\delta$-$MnO_2$), Fe-biomat system was responsible for the formation of Fe-oxides (hematite) and Fe-hydroxides (ferrihydrite and lepidocrocite). During the early diagenesis, manganese oxides reacted with the organic matter in the sediment through the microbially mediated processes and the Mn-metasomatism of the cyanobacterial carbonate jointly contributed to formation of early diagenetic manganese carbonate ore. The redox fluctuations between oxic/suboxic and anoxic conditions led to the re-oxidation process and resulted in cyclic marcasite. Anatase cycles observed in samples were interpreted as the diagenetic product of Fe-

biomat system.

## Declaration of Competing Interest

The authors declare that they have no known competing financial interests or personal relationships that could have appeared to influence the work reported in this paper.

## Acknowledgments

This study was supported by the Natural Science Foundation of China (No. U1812402 and No. 42072131), the Young Talent Project of the Department of Science and Technology of Guizhou Province (No. 2019-5654) and Research Project of Guizhou Bureau of Geology and Mineral Exploration and Development (2020-No.9). The authors thank the support of the National Research, Development and Innovation Office (Hungary), National Scientific Research Fund No. 125060. The comments of editor and anonymous reviewers are highly appreciated.

## Appendix A. Supplementary data

Supplementary data to this article can be found online at https://doi.org/10.1016/j.oregeorev.2021.104259.

## References

Baele, J.-M., Boulvain, F., De Jong, J., Matielli, N., Papier, S., Préat, A., 2008. Iron microbial mats in Modern and Phanerozoic environments. Proc SPIE 7097.

Bargar, J.R., Tebo, B.M., Bergmann, U., Webb, S.M., Glatzel, P., Chiu, V.Q., Villalobos, M., 2005. Biotic and abiotic products of Mn (II) oxidation by spores of the marine Bacillus sp. strain SG-1. Am. Min 90 (1), 143–154.

Baturin, G.N., 1988. In: The geochemistry of manganese and manganese nodules in the Ocean. Springer Netherlands, Dordrecht, pp. 45–57. https://doi.org/10.1007/978-94-009-3731-4_4.

Bgmrhnp, 1988. Regional Geology of the Guizhou Province (in Chinese with English abstract). Geological Press House, Beijing.

Biondi, J.C., Polgári, M., Gyollai, I., Fintor, K., Kovács, I., Fekete, J., Mojzsis, S.J., 2020. Biogenesis of the neoproterozoic kremydilite manganese ores from urucum (Brazil) – a new manganese ore type. Precambr. Res. 340, 105624. https://doi.org/10.1016/j.precamres.2020.105624.

Biondi, J.C., Lopez, M., 2017. Urucum Neoproterozoic-Cambrian manganese deposits (MS, Brazil): Biogenic participation in the ore genesis, geology, geochemistry, and depositional environment. Ore Geol. Rev. 91, 335–386.

Blöthe, M., Wegorzewski, A., Müller, C., Simon, F., Kuhn, T., Schippers, A., 2015. Manganese-cycling microbial communities inside deep-sea manganese nodules. Environ. Sci. Technol. 49 (13), 7692–7700.

Bodeï, S., Manceau, A., Geoffroy, N., Baronnet, A., Buatier, M., 2007. Formation of todorokite from vernadite in Ni-rich hemipelagic sediments. Geochim. Cosmochim. Acta 71 (23), 5698–5716.

Böttcher, M.E., 2011. Manganese (sedimentary carbonates and sulfides). In: Reitner, J., Thiel, V. (Eds.), Encyclopedia of Geobiology. Springer, Netherlands, Dordrecht, pp. 541–542.

Burke, I.T., Kemp, A.E.S., 2002. Microfabric analysis of Mn-carbonate laminae deposition and Mn-sulfide formation in the Gotland Deep, Baltic Sea. Geochim. Cosmochim. Acta 66 (9), 1589–1600.

Castanier, S., Le Métayer-Levrel, G., Perthuisot, J.-P., 1999. Ca-carbonates precipitation and limestone genesis— the microbiogeologist point of view. Sed. Geol. 126 (1-4), 9–23.

Day, M., Ramezani, J., Bowring, S., Sadler, P., Erwin, D., Abdala, F., Rubidge, B., 2015. When and how did the terrestrial mid-Permian mass extinction occur? Evidence from the tetrapod record of the Karoo Basin, South Africa. Proceedings. Biological sciences / The Royal Society 282.

Dupraz, C., Reid, R.P., Braissant, O., Decho, A.W., Norman, R.S., Visscher, P.T., 2009. Processes of carbonate precipitation in modern microbial mats. Earth Sci. Rev. 96 (3), 141–162.

Dupraz, C., Visscher, P.T., 2005. Microbial lithification in marine stromatolites and hypersaline mats. Trends Microbiol. 13 (9), 429–438.

Egger, M., Hagens, M., Sapart, C.J., Dijkstra, N., van Helmond, N.A.G.M., Mogollón, J.M., Risgaard-Petersen, N., van der Veen, C., Kasten, S., Riedinger, N., Böttcher, M.E., Röckmann, T., Jørgensen, B.B., Slomp, C.P., 2017. Iron oxide reduction in methane-rich deep Baltic Sea sediments. Geochim. Cosmochim. Acta 207, 256–276.

Ehrenreich, A., Widdel, F., 1994. Anaerobic oxidation of ferrous iron by purple bacteria, a new type of phototrophic metabolism. Appl. Environ. Microbiol. 60, 4517–4526.

Ehrlich, H.L., 2002. Geomicrobiology, 4th ed. Marcell Dekker Inc., pp. 183–274

Fan, D., Yang, P., 1999. Introduction to and classification of manganese deposits of China. Ore Geol. Rev. 15 (1-3), 1–13.

Gao, J., Yang, R., Xu, H., Zhang, X.u., Feng, K., Zheng, L., 2018. Genesis of Permian sedimentary manganese deposits in Zunyi, Guizhou Province, SW China: constraints from geology and elemental geochemistry. J. Geochem. Explor. 192, 142–154.

Glamoclija, M., Steele, A., Fries, M., Schieber, J., Voytek, M., Cockell, C., 2009. Association of anatase (TiO2) and microbes: Unusual fossilization effect or a potential biosignature? Geol. Soc. Am. Special Papers 458, 965–975.

Hallbeck, L., Pedersen, K., 1990. Culture parameters regulating stalk formation and growth rate of Gallionella ferruginea. Microbiology 136 (9), 1675–1680.

He, B., Xu, Y.-G., Guan, J.-P., Zhong, Y.-T., 2010. Paleokarst on the top of the Maokou Formation: Further evidence for domal crustal uplift prior to the Emeishan flood volcanism. Litho 119 (1-2), 1–9.

He, B., Xu, Y.-G., Huang, X.-L., Luo, Z.-Y., Shi, Y.-R., Yang, Q.-J., Yu, S.-Y., 2007. Age and duration of the Emeishan flood volcanism, SW China: Geochemistry and SHRIMP zircon U-Pb dating of silicic ignimbrites, post-volcanic Xuanwei Formation and clay tuff at the Chaotian section. Earth Planet. Sci. Lett. 255 (3-4), 306–323.

Herdianita, N.R., Browne, P.R.L., Rodgers, K.A., Campbell, K.A., 2000. Mineralogical and textural changes accompanying ageing of silica sinter. Miner. Deposita 35 (1), 48–62.

Isozaki, Y., Kawahata, H., Minoshima, K., 2007. The Capitanian (Permian) Kamura cooling event: the beginning of the Paleozoic-Mesozoic transition. Palaeoworld 16 (1-3), 16–30.

Isozaki, Y., Servais, T., 2018. The Hirnantian (Late Ordovician) and end-Guadalupian (Middle Permian) mass-extinction events compared. Lethaia 51, 173–186.

Isozaki, Y., Yao, J., Ji, Z., Saitoh, M., Kobayashi, N., Sakai, H., 2008. Rapid sea-level change in the Late Guadalupian (Permian) on the Tethyan side of South China: litho- and biostratigraphy of the Chaotian section in Sichuan. Proc. Japan Acad., Series B 84 (8), 344–353.

Jerram, D.A., Widdowson, M., Wignall, P.B., Sun, Y., Lai, X., Bond, D.P.G., Torsvik, T.H., 2016. Submarine palaeoenvironments during Emeishan flood basalt volcanism, SW China: Implications for plume–lithosphere interaction during the Capitanian, Middle Permian ('end Guadalupian') extinction event. Palaeogeogr. Palaeoclimatol. Palaeoecol. 441, 65–73.

Jin, Y.G., Zhang, J., Shang, Q.H., 1995. Pre-Lopingian catastrophic event of marine faunas. Acta Palaeontologica Sinca 34, 410–427 (In Chinese with English abstract).

Johnson, J.E., Savalia, P., Davis, R., Kocar, B.D., Webb, S.M., Nealson, K.H., Fischer, W. W., 2016a. Real-time manganese phase dynamics during biological and abiotic manganese oxide reduction. Environ. Sci. Technol. 50 (8), 4248–4258.

Johnson, J.E., Webb, S.M., Ma, C., Fischer, W.W., 2016b. Manganese mineralogy and diagenesis in the sedimentary rock record. Geochim. Cosmochim. Acta 173, 210–231.

Kofukuda, D., Isozaki, Y., Igo, H., 2014. A remarkable sea-level drop and relevant biotic responses across the Guadalupian-Lopingian (Permian) boundary in low-latitude mid-Panthalassa: irreversible changes recorded in accreted paleo-atoll limestones in Akasaka and Ishiyama, Japan. J. Asian Earth Sci. 82, 47–65.

Konhauser, K.O., Planavsky, N.J., Hardisty, D.S., Robbins, L.J., Warchola, T.J., Haugaard, R., Lalonde, S.V., Partin, C.A., Oonk, P.B.H., Tsikos, H., Lyons, T.W., Bekker, A., Johnson, C.M., 2017. Iron formations: a global record of Neoarchaean to Palaeoproterozoic environmental history. Earth Sci. Rev. 172, 140–177.

Konhauser, K.O., 1998. Diversity of bacterial iron mineralization. Earth Sci. Rev. 43 (3-4), 91–121.

Korte, C., Ullmann, C.V., 2018. Permian strontium isotope stratigraphy. Geol. Soc., London, Special Publications 450 (1), 105–118.

Liu, P., Liao, Y.C., Yin, K.H., Ye, D.S., Zhu, H., Han, Z.H., Yang, G.L., 2008. Hydrothermal sedimentary manganese deposits assosiated to volcanic activities—Permian manganese deposits in Guizhou. Geol. China 35, 992–1006 (In Chinese with English abstract).

Liu, Z.C., Wang, C., Zhang, Y.G., Fan, B., Chen, D., Wei, Z.Q., Cui, Z.Q., 2015. Geochemistry and ore genesis of Zunyi Mn deposit, Guizhou Province, China. Acta Mineral. Sinca 35, 481–488 (In Chinese with English abstract).

Liu, Z.C., Zhou, Q., Yan, J.X., Wang, Y., Chen, D., Zhong, Y.L., Qin, X.J., 2019. Structure of Zunyi rift basin in Guihzou Province during the Permian and its controlling on manganese deposits. J. Palaeogeogr. (Chinese Edition) 21, 517–526 (In Chinese with English abstract).

Mandernack, K.W., Post, J., Tebo, B.M., 1995. Manganese mineral formation by bacterial spores of the marine bacillus, Strain SG-1: Evidence for the direct oxidation of Mn (II) to Mn (IV). Geochim. Cosmochim. Acta 59 (21), 4393–4408.

Maynard, J.B. (Ed.), 1983. Geochemistry of Sedimentary Ore Deposits. Springer New York, New York, NY.

Maynard, J.B., 2014. Manganiferous sediments, rocks, and ores. In: Treatise on Geochemistry. Elsevier, pp. 327–349.

Molnár, Z., Polgári, M., Hein, J.R., Józsa, S., Fekete, J., Gyollai, I., Fintor, K., Bíró, L., Szabó, M., Rapi, S., Forgó, P., Vigh, T., 2017. Fe-Mn oxide indications in the feeder and mound zone of the Jurassic Mn-carbonate ore deposit, Úrkút, Hungary. Ore Geol. Rev. 86, 839–855.

Murowchick, J.B., Barnes, H.L., 1986. Marcasite precipitation from hydrothermal solutions. Geochim. Cosmochim. Acta 50 (12), 2615–2629.

Polgári, M., Gyollai, I., 2021 current volume. Geochemical constraints on the element enrichments of microbially mediated manganese and iron ores – An overview.

Polgári, M., Gyollai, I., Fintor, K., Horváth, H., Elemér, P.-M., Biondi, J.C., 2019. Microbially mediated ore-forming processes and cell mineralization. Front. Microbiol. 10, 2731.

Polgári, M., Hein, J., Tóth, A., Pál-Molnár, E., Vigh, T., Bíró, L., Fintor, K., 2012a. Microbial action formed Jurassic Mn-carbonate ore deposit in only a few hundred years (Úrkút, Hungary). Geology 40, 903-906.

Polgári, M., Hein, J.R., Vigh, T., Szabó-Drubina, M., Fórizs, I., Bíró, L., Müller, A., Tóth, A.L., 2012b. Microbial processes and the origin of the Úrkút manganese deposit, Hungary. Ore Geol. Rev. 47, 87–109.

Polgári, M., Okita, P.M., Hein, J.R., 1991. Stable isotope evidence for the origin of the Úrkút manganese ore deposit. Hungary. J. Sed. Pet. 61 (3), 384–393.

Rampino, M.R., Shen, S.-Z., 2019. The end-Guadalupian (259.8 Ma) biodiversity crisis: the sixth major mass extinction? Hist. Biol. 33 (5), 716–722.

RRUFF Database. https://rruff.info/.

Schieber, J., 2011. Iron sulfide formation. In: Reitner, J., Thiel, V. (Eds.), Encyclopedia of Geobiology. Springer, Netherlands, Dordrecht, pp. 486–502.

Schoonen, M.A.A., Barnes, H.L., 1991. Reactions forming pyrite and marcasite from solution: I. Nucleation of FeS2 below 100°C. Geochim. Cosmochim. Acta 55 (6), 1495–1504.

Shellnutt, J.G., 2014. The Emeishan large igneous province: a synthesis. Geosci. Front. 5 (3), 369–394.

Shellnutt, J.G., Pham, T.T., Denyszyn, S.W., Yeh, M.-W., Tran, T.-A., 2020. Magmatic duration of the Emeishan large igneous province: Insight from northern Vietnam. Geology 48, 457–461.

Shi, L., Feng, Q., Shen, J., Ito, T., Chen, Z.-Q., 2016. Proliferation of shallow-water radiolarians coinciding with enhanced oceanic productivity in reducing conditions during the Middle Permian, South China: evidence from the Gufeng Formation of western Hubei Province. Palaeogeogr. Palaeoclimatol. Palaeoecol. 444, 1–14.

Straub, K.L., Benz, M., Schink, B., Widdel, F., 1996. Anaerobic, nitrate-dependent microbial oxidation of ferrous iron. Appl. Environ. Microbiol. 62, 1458–1460.

Vandieken, V., Pester, M., Finke, N., Hyun, J.-H., Friedrich, M.W., Loy, A., Thamdrup, B. o., 2012. Three manganese oxide-rich marine sediments harbor similar communities of acetate-oxidizing manganese-reducing bacteria. ISME J. 6 (11), 2078–2090.

Villalobos, M., Toner, B., Bargar, J., Sposito, G., 2003. Characterization of the manganese oxide produced by pseudomonas putida strain MnB1. Geochim. Cosmochim. Acta 67 (14), 2649–2662.

Wang, Y., Peate, I.U., Luo, Z., Wang, S., Cheng, L., Hao, J., Wang, Y., 2018. Rifting in SW China: structural and sedimentary investigation of the initial crustal response to emplacement of the Permian Emeishan LIP. Geol. Mag. 156 (4), 745–758.

Wittkop, C., Swanner, E.D., Grengs, A., Lambrecht, N., Fakhraee, M., Myrbo, A., Bray, A. W., Poulton, S.W., Katsev, S., 2020. Evaluating a primary carbonate pathway for manganese enrichments in reducing environments. Earth Planet. Sci. Lett. 538, 116201. https://doi.org/10.1016/j.epsl.2020.116201.

Xu, H., Gao, J., Yang, R., Du, L., Liu, Z., Chen, J., Feng, K., Yang, G., 2019. Genesis for Rare Earth Elements Enrichment in the Permian Manganese Deposits in Zunyi, Guizhou Province, SW China. Acta Geologica Sinica - English Edition.

Xu, H., Gao, J., Yang, R., Feng, K., Wang, L., Chen, J., 2021. Metallogenic mechanism of large manganese deposits from Permian manganese ore belt in western South China Block: new mineralogical and geochemical evidence. Ore Geol. Rev. 132, 103993. https://doi.org/10.1016/j.oregeorev.2021.103993.

Xu, Y.-G., Luo, Z.-Y., Huang, X.-L., He, B., Xiao, L., Xie, L.-W., Shi, Y.-R., 2008. Zircon U-Pb and Hf isotope constraints on crustal melting associated with the Emeishan mantle plume. Geochim. Cosmochim. Acta 72 (13), 3084–3104.

Yan, H., Pi, D.-H., Jiang, S.-Y., Hao, W., Mänd, K., Robbins, L.J., Li, L., Konhauser, K.O., 2020. New constraints on the onset age of the Emeishan LIP volcanism and implications for the Guadalupian mass extinction. Litho 360-361, 105441. https://doi.org/10.1016/j.lithos.2020.105441.

Yu, W., Algeo, T.J., Du, Y., Zhou, Q.i., Wang, P., Xu, Y., Yuan, L., Pan, W., 2017. Newly discovered Sturtian cap carbonate in the Nanhua Basin, South China. Precambr. Res. 293, 112–130.

Yu, W., Algeo, T.J., Yan, J., Yang, J., Du, Y., Huang, X., Weng, S., 2019a. Climatic and hydrologic controls on upper Paleozoic bauxite deposits in South China. Earth Sci. Rev. 189, 159–176.

Yu, W., Polgári, M., Fintor, K., Gyollai, I., Huang, H., Szabó, M., Du, Y., 2021 current volume. Microbial metallogenesis of Early Carboniferous manganese deposit in central Guangxi, South China.

Yu, W., Polgári, M., Gyollai, I., Fintor, K., Szabó, M., Kovács, I., Fekete, J., Du, Y., Zhou, Q.i., 2019b. Microbial metallogenesis of Cryogenian manganese ore deposits in South China. Precambr. Res. 322, 122–135.

Zhong, H., Zhu, W.-G., Chu, Z.-Y., He, D.-F., Song, X.-Y., 2007. Shrimp U-Pb zircon geochronology, geochemistry, and Nd–Sr isotopic study of contrasting granites in the Emeishan large igneous province, SW China. Chem. Geol. 236 (1-2), 112–133.

Zhu, B., Guo, Z., Zhang, S., Ukstins, I., Du, W., Liu, R., 2019. What triggered the early-stage eruption of the Emeishan large igneous province? GSA Bulletin 131, 1837–1856.